On the conformity of strong, regularized, embedded and smeared discontinuity approaches for the modeling of localized failure in solids

Miguel Cervera[a], Jian-Ying Wu[b,*]

[a]CIMNE, Technical University of Catalonia, Edificio C1, Campus Norte, Jordi Girona 1-3, 08034 Barcelona, Spain.
[b]State Key Laboratory of Subtropic Buildig Science, South China University of Technology, 510641 Guangzhou, China.

Abstract

Once strain localization occurs in softening solids, inelastic loading behavior is restricted within a narrow band while the bulk unloads elastically. Accordingly, localized failure in solids can be approached by embedding/smearing a traction-based inelastic discontinuity (band) within an (equivalent) elastic matrix along a specific orientation. In this context, the conformity of the strong/regularized and embedded/smeared discontinuity approaches are investigated, regarding the strategies dealing with the kinematics and statics. On one hand, the traction continuity condition imposed in weak form results in the strong and regularized discontinuity approaches, with respect to the approximation of displacement/strain discontinuities. In addition to the elastic bulk, consistent plastic-damage cohesive models for the discontinuities are established. The conformity between the strong discontinuity approach and its regularized counterpart is shown through the fracture energy analysis. On the other hand, the traction continuity condition can also be enforced point-wisely in strong form so that the standard principle of virtual work applies. In this case, the static constraint resulting from traction continuity can be used to eliminate the kinematic variable associated with the discontinuity (band) at the material level. This strategy leads to embedded/smeared discontinuity models for the overall weakened solid which can also be cast into the elastoplastic degradation framework with a different kinematic decomposition. Being equivalent to the kinematic constraint guaranteeing stress continuity upon strain localization, Mohr's maximization postulate is adopted for the determination of the discontinuity orientation. Closed-form results are presented in plane stress conditions, with the classical Rankine, Mohr-Coulomb, von Mises and Drucker-Prager criteria as illustrative examples. The orientation of the discontinuity (band) and the stress-based failure criteria consistent with the traction-based counterparts are given. Finally, a generic failure criterion of either elliptic, parabolic or hyperbolic type, appropriate for the modeling of mixed-mode failure, is analyzed in a unified manner. Furthermore, a novel method is proposed to calibrate the involved mesoscopic parameters from available macroscopic test data, which is then validated against Willam's numerical test.

Keywords:
Fracture, plasticity, damage, strong and regularized discontinuities, embedded and smeared cracks

---

[*] Tel.: (+86) 20-87112787
Email address: `jywu@scut.edu.cn` (Jian-Ying Wu)

May 4, 2015

1. Introduction

Deformation in solids with an overall softening response is characterized with strain localization leading to their final failure. Being a manifestation of concentration of micro-structural defects, typical examples include cracks in concrete, joints in rocks, shear bands in soils, dislocations and slip lines in metals, etc. Structural collapse is often the consequence of such localized failure, prognosticated by the formation of localization bands of small width or even fracture surfaces of negligible width compared to the length scale of the structure considered. Therefore, it is of utmost significance to evaluate (residual) structural safety once strain localization occurs, and to prevent potential catastrophic structural collapse caused by localized failure.

The onset of strain localization inevitably induces strain/displacement discontinuities and the standard kinematics of a continuum medium no longer applies (Thomas, 1961). Furthermore, once strain localization occurs in softening solids, the dissipative mechanisms and the induced nonlinear behavior are completely restricted within the localization band while the bulk outside it unloads elastically (Oliver et al, 1999; Cervera et al., 2012). For the unloading behavior, the bulk can be regarded as an equivalent elastic medium described by classical (tensorial) constitutive relations in terms of stresses *versus* strains (Chen, 1994; Krajcinovic, 2003), in which inelastic responses proceeding strain localization can be incorporated as well. Being its orientation known or determined, the discontinuity (band) can be sufficiently described by a (vectorial) cohesive model with a traction-based failure criterion and appropriate evolution laws. The traction continuity condition applies between the discontinuity (band) and the bulk, leading to an overall response of intrinsic anisotropy. In this context, localized failure in softening solids can be approached by *a traction-based inelastic discontinuity (band) localized within an (equivalent) elastic matrix along a specific orientation* (Wu and Cervera, 2014b).

Within the above methodology, different approaches have been proposed for the modeling of localized failure in solids (Ngo and Scordelis, 1967; Rashid, 1968). These approaches differ mainly in the approximation of the kinematics (displacement and strain fields) and statics (stress field and traction continuity) in the discontinuity (band). Displacement or strong discontinuities are regarded as zero-width interfaces which are characterized by a cohesive model in terms of tractions *versus* displacement jumps (Barenblatt, 1959, 1962; Dugdale, 1960; Hillerborg et al., 1976). Alternatively, strain or weak discontinuities limiting the localized band with a finite width can be represented by a regularized cohesive model in terms of tractions *versus* inelastic deformations (i.e., apparent displacement jumps normalized with respect to the bandwidth) (Cervera, 2008a,b). Depending on the recoverable/irreversible properties of the discontinuities upon unloading, cohesive models of either plastic (Stankowski et al., 1993; Cervenka, 1994; Carol et al., 1997; Weihe et al., 1997), damage (Armero, 1999; Armero and Oller, 1998; Jirásek and Zimmermann, 2001) or combined plastic-damage (Wu and Xu, 2011; Wu, 2011) type can be established. Similarly to the tensorial constitutive laws, irreversible thermodynamics with internal variables (Coleman and Gurtin, 1967) is usually employed to guarantee the consistency of the cohesive model.

The discontinuity (band) is localized in the bulk through the in-between traction continuity condition. This static condition on the discontinuity can be imposed in either weak or strong form. In an integral sense, the weak form explicitly accounts for the displacement/strain discontinuities in such a way that the kinematic variables associated with the discontinuity (band) are retained. The resulting boundary value problem is no longer standard in the sense that the internal virtual work consists of contributions from both the bulk and the discontinuity (band) (Malvern, 1969; Wu, 2011). Accordingly, constitutive relations for both the bulk and the discontinuity (band) have to be provided. Contrariwise, if the traction continuity condition is enforced point-wisely in strong form, it is possible to eliminate the kinematic variables on the material level (Rots, 1985, 1988; Armero and Oller, 1998). In this case, the displacement/strain discontinuities are implicitly accounted for and the standard principle of virtual work applies. Accordingly, a single inelastic constitutive model for the overall weakened solid suffices for this strategy.

As mentioned before, a traction-based failure criterion with appropriate softening laws is adopted to characterize the inelastic discontinuity (band). The Rankine criterion is generally employed in the modeling of mode-I failure. For mixed mode failure, it is difficult to quantify the interaction between normal and tangential responses on the discontinuity surface. This fact brings about two problems, i.e., (i) the linear Mohr-Coulomb criterion is in general insufficient and more complex models have to be considered, and (ii) even if the failure criterion is postulated, usually in an *ad hoc* manner, it is hard to calibrate the involved parameters. For instance, either elliptical (Camacho and Ortiz, 1996; Pandolfi et al., 1999; Jirásek and Zimmermann, 2001; Wu and Xu, 2011), parabolic (Ohlsson and Olofsson, 1997; Mosler, 2005) or hyperbolic (Carol et al., 1997; Cervenka, 1994; Weihe et al., 1997; Most and Bucher, 2007) functions have been postulated to describe mixed-mode failure in quasi-brittle materials. However, the involved parameters are essentially mesoscopical entities hard to determine from rather limited experimental data. This shortcoming restrains heavily the predictive capability of traction-based approaches. The scenario is quite different for stress-based material failure criteria which prescribe an admissible domain of stress states. Extensive experimental data make it possible to postulate appropriate stress-based failure criteria and calibrate the model parameters, especially for concrete-like quasi-brittle materials (Chen, 1994).

In traction-based approaches for the modeling of localized failure in solids, an indispensable step is to determine the orientation of the discontinuity (band). It is assumed *a priori* that the discontinuity (band) forms, and the question is whether the expected strain localization can occur and, if it can, what is the orientation. The above tasks cannot be easily resolved, especially for a new or propagating discontinuity whose orientation is not pre-defined or known *a priori*. To this end, *ad hoc* strategies have to be introduced, usually in an heuristic manner. For instance, the Rankine criterion based on the bulk stresses is often adopted for mode-I failure in quasi-brittle solids. Mohr's maximization postulate has been employed occasionally in the literature (Ottosen and Runesson, 1991b; Weihe et al., 1997) to determine the discontinuity orientation for general traction-based mixed-mode failure criterion, but its rationality has not been fully justified. For an inelastic bulk, the singularity condition of the acoustic tensor, necessary for discontinuous bifurcation, has been widely adopted to determine the orientation of shear bands observed in elastoplatic materials; see (Rudnicki and Rice, 1975; Rice and Rudnicki, 1980; Ottosen and Runesson, 1991a; Runesson et al., 1991; Steinmann and Willam, 1991) and the references therein. The discontinuous bifurcation condition with perfect (null) softening/hardening modulus was also suggested by Simó et al. (1993) and Oliver (1996) to determine the orientation of a strong discontinuity in softening solids. Despite its generality at the cost of a considerable computational overhead, it is worth noting that, for the above discontinuous bifurcation analysis, (i) the underlying assumption of a linear comparison solid (inelastic loading state both inside and outside the localization band) (Hill, 1958, 1962) is not consistent with the stress states upon strain localization in softening solids; (ii) being only a necessary one, the said condition guarantees neither the occurrence of a strong discontinuity in general cases (Oliver et al., 1998; Oliver et al, 1999) nor its eventual evolution into a fully softened discontinuity; (iii) it cannot be used for the elastic bulk since the acoustic tensor is always regular and, for the inelastic bulk characterized by a stress-based model, the traction-based counterpart for the discontinuity (band) in general cannot be given explicitly. The above arguments make the classical strain localization analysis questionable as a general tool for softening solids.

It follows from distributional analysis (Simó et al., 1993; Oliver, 1996, 2000) that, due to the singular strain field around a strong discontinuity, traction continuity alone is not sufficient to guarantee physically meaningful results, but rather, stress boundedness also has to be invoked (Simó et al., 1993; Oliver, 1996; Oliver et al., 1998; Oliver et al, 1999; Oliver, 2000). Noticing this fact, Cervera et al. (2012) used the kinematic compatibility condition resulting from stress boundedness to determine the discontinuity orientation, so that the stress locking-free property can be guaranteed for a fully softened discontinuity. More recently, the authors (Wu and Cervera, 2013, 2014a,b) show that upon strain localization the stress field not only is bounded, but also is continuous, provided *only the discontinuity modes caused by relative rigid body motions (translations and rotations) are considered* (Wu, 2011; Wu et al., 2015). This condition is more demanding than the classical bifurcation condition that implies singularity of the acoustic tensor and the corresponding loss of material ellipticity (Rudnicki and Rice, 1975; Rice and Rudnicki, 1980; Runesson et al., 1991). Based on the more stringent stress continuity condition, a novel strain localization analysis has recently been proposed (Wu and Cervera, 2014b). Not only the discontinuity orientation but also the traction-based failure criterion are determined consistently from a stress-based inelastic material model. Accordingly, localized failure in solids can be approached from an alternative methodology, i.e., *stress continuity based strain localization of an inelastic solid*. Results obtained with this methodology do not necessarily coincide with those of classical localization analysis. For instance, the discontinuity orientation does not depend on the value of an elastic property such as Poisson's ratio. Furthermore, the bi-directional connections between traction- and stress-based approaches are established.

Trying to make further contributions to the above topics, the objectives of this work are fourfold: (a) to classify the existing traction-based approaches and to clarify their in-between connections, (b) to exploit the use of the conformity between traction- and stress-based approaches for the determination of the discontinuity orientation and the calibration of the model parameters, (c) to present closed-form results of several classical models in plane stress conditions, and (d) to advocate a generic traction-based criterion appropriate for the modeling of mixed-mode failure. These connections are not at all evident in general cases.

The scope of the paper is restricted to the continuum setting. The interrelation with possible finite element approximations in the discrete setting is not covered in this work. Strong discontinuities, with discontinuous displacement fields, may be approximated using the XFEM method (Moës et al., 1999; Wells and Sluys, 2001) or the "continuum strong discontinuity approach" (Simó et al., 1993; Oliver, 1996; Jirásek and Zimmermann, 2001). These numerical methods to approximate discontinuities differ mainly in the enhanced discrete approximation of the (regularized or not) displacement jumps at the discontinuity; see Wu (2011); Wu et al. (2015) for more discussion.

This paper is organized as follows. After this introduction, in Section 2 the strong and regularized discontinuity approaches are discussed, focusing on the kinematics, governing equations, consistent constitutive laws and fracture energy, respectively. Section 3 addresses the embedded and smeared discontinuity approaches, in which elastoplastic damage models for the overall weakened solid are established within two alternative frameworks. Section 4 is devoted to the determination of the discontinuity orientation in general 3D cases, together with the closed-form results and several prototype examples in plane stress conditions. As an application, in Section 5 a generic traction-based failure criterion, appropriate for the modeling of mixed-mode failure in solids, is analyzed. Furthermore, a new method to calibrate the involved parameters is presented and then validated against Willam's numerical test. The relevant conclusions drawn in Section 6 close the paper.

Notation. Compact tensor notation is used in this paper as much as possible. As a general rule, scalars are denoted by italic light-face Greek or Latin letters (e.g. a or λ); vectors and second-order tensors are signified by italic boldface minuscule and majuscule letters like $\boldsymbol{a}$ and $\boldsymbol{A}$, respectively. Fourth-order tensors are identified by blackboard-bold majuscule characters (e.g. $\mathbb{A}$). Symbols $\boldsymbol{I}$ and $\mathbb{I}$ represent the second-order and fourth-order symmetric identity tensors, respectively. Superscripts '$^{\mathrm{T}}$' and '$^{\mathrm{sym}}$' indicate the transposition and symmetrization operations, respectively. The inner products with single and double contractions are denoted by '$\cdot$' and '$:$', respectively. The dyadic product '$\otimes$' and symmetrized Kronecker product $\overline{\underline{\otimes}}$ are defined as

$$(\boldsymbol{A} \otimes \boldsymbol{B})_{ijkl} = A_{ij} B_{kl}, \qquad (\boldsymbol{A} \overline{\underline{\otimes}} \boldsymbol{B})_{ijkl} = \frac{1}{2}\big(A_{ik} B_{jl} + A_{il} B_{jk}\big)$$

for two arbitrary second-order tensors $\boldsymbol{A}$ and $\boldsymbol{B}$.

2. Strong/regularized discontinuity approaches

As shown in Fig. 1, the domain $\Omega \subset \mathbb{R}^{n_{\mathrm{dim}}}$ ($n_{\mathrm{dim}} = 1, 2, 3$) occupied by a solid with reference position vector $\boldsymbol{x} \in \mathbb{R}^{n_{\mathrm{dim}}}$ is considered. The boundary of the domain Ω is denoted by $\Gamma \subset \mathbb{R}^{n_{\mathrm{dim}}-1}$, with an external unit normal vector $\boldsymbol{n}^{*}$. Deformations of the solid are characterized by the displacement field $\boldsymbol{u} : \Omega \to \mathbb{R}^{n_{\mathrm{dim}}}$ and the infinitesimal strain field $\boldsymbol{\epsilon} = \nabla^{\mathrm{sym}} \boldsymbol{u} : \Omega \to \mathbb{R}^{n_{\mathrm{dim}} \times n_{\mathrm{dim}}}$, with $\nabla(\cdot)$ being the spatial gradient operator.

Upon satisfaction of a specified criterion, an internal surface $\mathcal{S}$ is introduced, with the orientation characterized by a unit normal vector $\boldsymbol{n}$, fixed along time (i.e., $\dot{\boldsymbol{n}} = \boldsymbol{0}$) and pointing from Ω^{-} to Ω^{+}. The interface $\mathcal{S}$ splits the solid Ω into two sub-domains Ω^{+} and Ω^{-}, i.e., $\Omega = \Omega^{+} \cup \Omega^{-} \cup \mathcal{S}$. Consequently, the displacement and strain fields no longer remain continuous and may be discontinuous or even singular at the interface $\mathcal{S}$.

2.1. Governing equations

The solid is subjected to the body forces (per unit volume) $\boldsymbol{b}^* : \Omega \to \mathbb{R}^{n_{\text{dim}}}$ distributed in the domain Ω and surface tractions $\boldsymbol{t}^* : \Gamma_t \to \mathbb{R}^{n_{\text{dim}}}$ applied on a portion of the boundary $\Gamma_t \subset \Gamma$. The prescribed displacements imposed on the complementary boundary $\Gamma_u \subset \Gamma$ are denoted by $\boldsymbol{u}^* : \Gamma_u \to \mathbb{R}^{n_{\text{dim}}}$. Note that the boundaries Γ_u and Γ_t are disjointed, i.e., $\Gamma_u \cap \Gamma_t = \emptyset$ and $\overline{\Gamma_u \cup \Gamma_t} = \Gamma$, so that the resulting boundary value problem is well-posed. Restricting the discussion to quasi-static loading, the governing equations are expressed as

$$\begin{aligned} &\text{Balance of linear momentum:} && \nabla \cdot \boldsymbol{\sigma} + \boldsymbol{b}^* = \boldsymbol{0} && \text{in } \Omega \backslash \mathcal{S} \\ &\text{Traction continuity condition:} && \boldsymbol{\sigma}_{\mathcal{S}}^{+} \cdot \boldsymbol{n} = \boldsymbol{\sigma}_{\mathcal{S}}^{-} \cdot \boldsymbol{n} = \boldsymbol{t} && \text{in } \mathcal{S} \end{aligned} \tag{2.1}$$

supplemented by the following boundary conditions

$$\begin{aligned} &\text{Traction boundary condition:} && \boldsymbol{\sigma} \cdot \boldsymbol{n}^* = \boldsymbol{t}^* && \text{in } \Gamma_t \\ &\text{Displacement boundary condition:} && \boldsymbol{u} = \boldsymbol{u}^* && \text{in } \Gamma_u \end{aligned} \tag{2.2}$$

where the second-order tensor $\boldsymbol{\sigma} : \Omega \backslash \mathcal{S} \to \mathbb{R}^{n_{\text{dim}} \times n_{\text{dim}}}$ denotes the stress field in the bulk $\Omega \backslash \mathcal{S} = \Omega^+ \cup \Omega^-$, with $\boldsymbol{\sigma}_{\mathcal{S}}^{+} := \boldsymbol{\sigma}(\boldsymbol{x} \in \Omega^+ \cap \mathcal{S})$ and $\boldsymbol{\sigma}_{\mathcal{S}}^{-} := \boldsymbol{\sigma}(\boldsymbol{x} \in \Omega^- \cap \mathcal{S})$ being the bulk stresses “ahead of” and “behind” the interface $\mathcal{S}$, respectively; the vector $\boldsymbol{t} : \mathcal{S} \to \mathbb{R}^{n_{\text{dim}}}$ denotes the cohesive traction transferred across the discontinuity $\mathcal{S}$.

2.2. Kinematics and weak forms

With respect to the strategy dealing with the discontinuity or singularity exhibited in the kinematics, either the strong discontinuity approach or the regularized one can be developed for the above boundary value problem.

2.2.1. Strong discontinuity approach

To describe the displacement jump $\boldsymbol{w} : \mathcal{S} \to \mathbb{R}^{\text{dim}}$, the Heaviside function $\mathscr{H}_{\mathcal{S}}(\boldsymbol{x})$ is introduced as $\mathscr{H}_{\mathcal{S}}(\boldsymbol{x}) = 1$ if $\boldsymbol{x} \in \Omega^+$ and $\mathscr{H}_{\mathcal{S}}(\boldsymbol{x}) = 0$ otherwise. Accordingly, the displacement field $\boldsymbol{u}(\boldsymbol{x})$ can be expressed as

$$\boldsymbol{u}(\boldsymbol{x}) = \bar{\boldsymbol{u}}(\boldsymbol{x}) + \mathscr{H}_{\mathcal{S}}(\boldsymbol{x})\, \hat{\boldsymbol{u}}(\boldsymbol{x}) \tag{2.3a}$$

and the resulting strain field $\boldsymbol{\epsilon}(\boldsymbol{x})$ is given by

$$\boldsymbol{\epsilon}(\boldsymbol{x}) = \nabla^{\text{sym}} \bar{\boldsymbol{u}}(\boldsymbol{x}) + \big(\boldsymbol{w} \otimes \boldsymbol{n}\big)^{\text{sym}}\, \delta_{\mathcal{S}}(\boldsymbol{x}) \tag{2.3b}$$

where $\delta_{\mathcal{S}}(\boldsymbol{x})$ is the Dirac-delta defined at the interface $\mathcal{S}$; $\bar{\boldsymbol{u}}(\boldsymbol{x})$ denotes the continuous displacement field in the solid; the relative displacement field $\hat{\boldsymbol{u}}(\boldsymbol{x}) : \Omega \to \mathbb{R}^{n_{\text{dim}}}$, satisfying the property $\hat{\boldsymbol{u}}(\boldsymbol{x} \in \mathcal{S}) = \boldsymbol{w}$, describes how the sub-domain Ω^+ moves as a rigid body (e.g., translations and rotations) with respect to the other sub-domain Ω^-; see Wu (2011). If only rigid body translations are considered, the relative displacement field $\hat{\boldsymbol{u}}(\boldsymbol{x})$ is constant along the interface $\mathcal{S}$ and its magnitude coincides with the displacement jump $\boldsymbol{w}$. Note that, though the relative displacement field $\hat{\boldsymbol{u}}(\boldsymbol{x})$ is not necessarily constant, its contribution to the strain field vanishes, i.e., $\nabla^{\text{sym}} \hat{\boldsymbol{u}}(\boldsymbol{x}) = \boldsymbol{0}$.

As can be seen, the strong discontinuity $\mathcal{S}$ induces a discontinuous (or $\mathcal{C}^{-1}$-continuous) displacement field $\boldsymbol{u}(\boldsymbol{x})$ and a singular (unbounded) strain field $\boldsymbol{\epsilon}(\boldsymbol{x})$; see Fig. 2. With the singular kinematics (2.3), the governing equation (2.1) and the traction boundary condition $(2.2)_1$ can be cast into the following weak form for the *strong discontinuity approach* (Malvern, 1969)

$$\int_{\Omega} \nabla^{\text{sym}} \delta \boldsymbol{u} : \boldsymbol{\sigma} \, \mathrm{d}\Omega = \int_{\Omega\backslash\mathcal{S}} \nabla^{\text{sym}} \delta \bar{\boldsymbol{u}} : \boldsymbol{\sigma} \, \mathrm{d}\Omega + \int_{\mathcal{S}} \delta \boldsymbol{w} \cdot \boldsymbol{t} \, \mathrm{d}\mathcal{S} = \int_{\Omega} \delta \boldsymbol{u} \cdot \boldsymbol{b}^* \, \mathrm{d}\Omega + \int_{\Gamma_t} \delta \boldsymbol{u} \cdot \boldsymbol{t}^* \, \mathrm{d}\Gamma \tag{2.4}$$

where the trial function $\boldsymbol{u} \in \mathscr{U}$ and its variation $\delta\boldsymbol{u} \in \mathcal{V}$ are chosen within the spaces

$$\mathscr{U} := \Big\{ \boldsymbol{u} \big| \boldsymbol{u} = \bar{\boldsymbol{u}} + \mathscr{H}_{\mathcal{S}} \, \hat{\boldsymbol{u}}; \ \boldsymbol{u} = \boldsymbol{u}^* \text{ in } \Gamma_u; \Big\} \tag{2.5a}$$

$$\mathcal{V} := \Big\{ \delta\boldsymbol{u} \big| \delta\boldsymbol{u} = \delta\bar{\boldsymbol{u}} + \mathscr{H}_{\mathcal{S}} \, \delta\hat{\boldsymbol{u}}; \ \delta\boldsymbol{u} = \boldsymbol{0} \text{ in } \Gamma_u \Big\} \tag{2.5b}$$

for the variations $\delta\bar{\boldsymbol{u}}$ and $\delta\hat{\boldsymbol{u}}$ of sufficient regularity. Note that the displacement boundary conditions $(2.2)_2$ are usually enforced in strong form.

2.2.2. *Regularized discontinuity approach*

Alternatively, the interface $\mathcal{S}$ may be approximated by a regularized discontinuity (or discontinuity band) $\mathcal{B}$, delimited by two surfaces $\mathcal{S}^+$ and $\mathcal{S}^-$ parallel to $\mathcal{S}$, i.e., $\Omega^+ \cup \Omega^- \cup \mathcal{B} = \Omega$; see Fig. 3(a). In this case, the discontinuous displacement field (2.3a) can be approximated by

$$\boldsymbol{u}(\boldsymbol{x}) = \bar{\boldsymbol{u}}(\boldsymbol{x}) + \mathscr{H}_{\mathcal{B}}(\boldsymbol{x}) \, \hat{\boldsymbol{u}}(\boldsymbol{x}) \tag{2.6a}$$

where the ramp function $\mathscr{H}_{\mathcal{B}}(\boldsymbol{x})$ is defined as $\mathscr{H}_{\mathcal{B}}(\boldsymbol{x}) = 0$ if $\boldsymbol{x} \in \Omega^-$, $\mathscr{H}_{\mathcal{B}}(\boldsymbol{x}) = 1$ if $\boldsymbol{x} \in \Omega^+$ and $\mathscr{H}_{\mathcal{B}}(\boldsymbol{x}) = \frac{1}{b}\big(\boldsymbol{x} - \boldsymbol{x}^*\big) \cdot \boldsymbol{n}$ if $\boldsymbol{x} \in \mathcal{B}$, with $\boldsymbol{x}^*$ being the spatial coordinates of point $\boldsymbol{x}$ projected along the direction $-\boldsymbol{n}$ to the surface $\mathcal{S}^-$. Note that the regularization parameter b, not necessarily a physical length, can be made as small as desired. Accordingly, the singular strain field (2.3b) is regularized as

$$\boldsymbol{\epsilon}(\boldsymbol{x}) = \nabla^{\text{sym}} \bar{\boldsymbol{u}}(\boldsymbol{x}) + \big(\boldsymbol{e} \otimes \boldsymbol{n}\big)^{\text{sym}} \, \Xi_{\mathcal{B}}(\boldsymbol{x}) \tag{2.6b}$$

where $\Xi_{\mathcal{B}}(\boldsymbol{x})$ denotes the collocation function within the discontinuity band $\mathcal{B}$, i.e., $\Xi_{\mathcal{B}}(\boldsymbol{x}) = 1$ if $\boldsymbol{x} \in \mathcal{B}$ and $\Xi_{\mathcal{B}}(\boldsymbol{x}) = 0$ otherwise; $\boldsymbol{e} := \boldsymbol{w}/b$ represents the deformation vector, with $\boldsymbol{w} := \boldsymbol{u}(\boldsymbol{x} \in \Omega^+ \cap \mathcal{B}) - \boldsymbol{u}(\boldsymbol{x} \in \Omega^- \cap \mathcal{B})$ now being the *apparent* displacement jump across the discontinuity band $\mathcal{B}$.

As shown in Fig. 3(b), the kinematic of a regularized discontinuity is characterized by a continuous displacement field $\boldsymbol{u}(\boldsymbol{x})$ and a regular (bounded) strain field $\boldsymbol{\epsilon}(\boldsymbol{x})$. Consistent with the above kinematics, the following weak form is obtained for the *regularized discontinuity approach*

$$\int_{\Omega} \nabla^{\text{sym}} \delta \boldsymbol{u} : \boldsymbol{\sigma} \, \mathrm{d}\Omega = \int_{\Omega\backslash\mathcal{B}} \nabla^{\text{sym}} \delta \bar{\boldsymbol{u}} : \boldsymbol{\sigma} \, \mathrm{d}\Omega + \int_{\mathcal{B}} \delta \boldsymbol{e} \cdot \boldsymbol{t} \, \mathrm{d}\mathcal{B} = \int_{\Omega} \delta \boldsymbol{u} \cdot \boldsymbol{b}^* \, \mathrm{d}\Omega + \int_{\Gamma_t} \delta \boldsymbol{u} \cdot \boldsymbol{t}^* \, \mathrm{d}\Gamma \tag{2.7}$$

where the trial function $\boldsymbol{u} \in \mathscr{U}$ and its variation $\delta\boldsymbol{u} \in \mathcal{V}$ are chose within the spaces

$$\mathscr{U} := \Big\{ \boldsymbol{u} \big| \boldsymbol{u} = \bar{\boldsymbol{u}} + \mathscr{H}_{\mathcal{B}} \, \hat{\boldsymbol{u}}; \ \boldsymbol{u} = \boldsymbol{u}^* \text{ in } \Gamma_u; \Big\} \tag{2.8a}$$

$$\mathcal{V} := \Big\{ \delta\boldsymbol{u} \big| \delta\boldsymbol{u} = \delta\bar{\boldsymbol{u}} + \mathscr{H}_{\mathcal{B}} \, \delta\hat{\boldsymbol{u}}; \ \delta\boldsymbol{u} = \boldsymbol{0} \text{ in } \Gamma_u \Big\} \tag{2.8b}$$

Note that for the regularized discontinuity with a vanishing band width $b \to 0$, the weak form (2.4) of the strong discontinuity approach is recovered.

Remark 2.1 As our main intention focuses on the nonlinear behavior lumped in the discontinuity, only linear elastic bulk materials are considered in this work; see Wu and Cervera (2014b) for the strategy dealing with nonlinear bulks. Upon the above methodology, the singular strain field (2.3b) and the regularized one (2.6b) can be expressed as

$$\boldsymbol{\epsilon}(\boldsymbol{x}) = \boldsymbol{\epsilon}^{\mathrm{e}}(\boldsymbol{x}) + \boldsymbol{\epsilon}^{\mathrm{in}}(\boldsymbol{x}) \tag{2.9}$$

where $\boldsymbol{\epsilon}^{\mathrm{e}}(\boldsymbol{x}) = \nabla^{\mathrm{sym}}\bar{\boldsymbol{u}}(\boldsymbol{x})$ represents the elastic strain field; the inelastic strain field $\boldsymbol{\epsilon}^{\mathrm{in}}(\boldsymbol{x})$ is given by

$$\boldsymbol{\epsilon}^{\mathrm{in}}(\boldsymbol{x}) = \big(\boldsymbol{w} \otimes \boldsymbol{n}\big)^{\mathrm{sym}}\, \delta_{\mathcal{S}}(\boldsymbol{x}) \qquad \text{or} \qquad \boldsymbol{\epsilon}^{\mathrm{in}}(\boldsymbol{x}) = \big(\boldsymbol{e} \otimes \boldsymbol{n}\big)^{\mathrm{sym}}\, \varXi_{\mathcal{B}}(\boldsymbol{x}) \tag{2.10}$$

Note that, though the total strain field may be discontinuous or even singular, the elastic one is continuous. □

2.3. *Cohesive model for strong and regularized discontinuities*

In the strong/regularized discontinuity approaches, the traction continuity condition $(2.1)_2$ is enforced in weak form such that the kinematic variable $\boldsymbol{w}$ (or $\boldsymbol{e} := \boldsymbol{w}/b$) associated to the discontinuity (band) is retained. In order to solve the boundary value problem (2.4) or (2.7), besides the elastic constitutive relation for the bulk, it is necessary to provide appropriate constitutive laws to determine the cohesive traction vector $\boldsymbol{t}$.

For the strong/regularized discontinuities, thermodynamically consistent cohesive models are developed in Wu and Cervera (2014b). Here, only the necessary formulas are summarized in Table 1 and all the derivations are omitted.

In the kinematic decompositions (2.11) and (2.12), the displacement jump $\boldsymbol{w}$ (or the inelastic deformation vector $\boldsymbol{e}$) is split into a recoverable damage part $\boldsymbol{w}^{\mathrm{d}}$ (or $\boldsymbol{e}^{\mathrm{d}}$) and an unrecoverable plastic one $\boldsymbol{w}^{\mathrm{p}}$ (or $\boldsymbol{e}^{\mathrm{p}}$). Accordingly, both stiffness degradation and irreversible deformations induced by the discontinuity (band) can be accounted for in the constitutive relations (2.13) and (2.14), where the second-order tensors $\widetilde{\boldsymbol{E}}^{\mathrm{d}}$ and $\widetilde{\boldsymbol{C}}^{\mathrm{d}}$ (or, $\boldsymbol{E}^{\mathrm{d}}$ and $\boldsymbol{C}^{\mathrm{d}}$) denote the variable stiffness and compliance tensors of the discontinuity (band), respectively. In the rate forms (2.15) and (2.16), $\dot{\boldsymbol{w}}^{\mathrm{dis}}$ and $\dot{\boldsymbol{e}}^{\mathrm{dis}}$ represent the *dissipative displacement jump rate* and *dissipative deformation rate*, respectively, both meaningful only in rate sense; see Figs. 4 and 5. A material parameter $\xi \in [0, 1]$ is introduced to discriminate between damage and plastic contributions. Namely, the cases $\xi = 0$ and $\xi = 1$ correspond to cohesive models of pure plastic and pure damage types, respectively, while the intermediate value $\xi \in (0, 1)$ results in plastic-damage cohesive models.

Accordingly, the associated evolution laws (2.17) and (2.18) are characterized by the dissipative flow vector $\boldsymbol{\gamma} := \partial f/\partial \boldsymbol{t}$ and softening function $h := -\partial f/\partial q$, where a *traction-based* failure criterion $f(\boldsymbol{t}, q) \le 0$, is introduced in the Kuhn-Tucker loading/unloading conditions (2.19) and (2.20). Without loss of generality, let us consider the following homogeneous failure function $f(\boldsymbol{t}, q)$ of degree $M \ge 1$

$$f(\boldsymbol{t}, q) = \frac{1}{M}\big(\partial_{\boldsymbol{t}} f \cdot \boldsymbol{t} + \partial_q f \cdot q\big) = \frac{1}{M}\big(\boldsymbol{\gamma} \cdot \boldsymbol{t} - h \cdot q\big) \le 0 \tag{2.27}$$

where $q(\cdot)$ denotes the cohesive strength of the discontinuity (band), dependent on a displacement-like internal variable $\tilde{\kappa}$ (or a strain-like one κ). When the discontinuity (band) is inactive, i.e., $f(\boldsymbol{t}, q) < 0$, it follows that $\tilde{\lambda} = 0$

Table 1: Cohesive models for the discontinuity (band)

Cohesive model for the strong discontinuity	Cohesive model for the regularized discontinuity
Kinematic decomposition	Kinematic decomposition
$\boldsymbol{w} = \boldsymbol{w}^{\rm d} + \boldsymbol{w}^{\rm p}, \qquad \boldsymbol{\epsilon}^{\rm in} = \boldsymbol{\epsilon}^{\rm d} + \boldsymbol{\epsilon}^{\rm p}$ (2.11)	$\boldsymbol{e} = \boldsymbol{e}^{\rm d} + \boldsymbol{e}^{\rm p}, \qquad \boldsymbol{\epsilon}^{\rm in} = \boldsymbol{\epsilon}^{\rm d} + \boldsymbol{\epsilon}^{\rm p}$ (2.12)
Constitutive relations	Constitutive relations
$\boldsymbol{t} = \widetilde{\boldsymbol{E}}^{\rm d} \cdot \boldsymbol{w}^{\rm d} = \widetilde{\boldsymbol{E}}^{\rm d} \cdot \big(\boldsymbol{w} - \boldsymbol{w}^{\rm p}\big)$ (2.13a)	$\boldsymbol{t} = \boldsymbol{E}^{\rm d} \cdot \boldsymbol{e}^{\rm d} = \boldsymbol{E}^{\rm d} \cdot \big(\boldsymbol{e} - \boldsymbol{e}^{\rm p}\big)$ (2.14a)
$\boldsymbol{w}^{\rm d} = \boldsymbol{w} - \boldsymbol{w}^{\rm p} = \widetilde{\boldsymbol{C}}^{\rm d} \cdot \boldsymbol{t}$ (2.13b)	$\boldsymbol{e}^{\rm d} = \boldsymbol{e} - \boldsymbol{e}^{\rm p} = \boldsymbol{C}^{\rm d} \cdot \boldsymbol{t}$ (2.14b)
Rate form	Rate form
$\dot{\boldsymbol{t}} = \widetilde{\boldsymbol{E}}^{\rm d} \cdot \big(\dot{\boldsymbol{w}} - \dot{\boldsymbol{w}}^{\rm dis}\big), \quad \dot{\boldsymbol{w}} = \widetilde{\boldsymbol{C}}^{\rm d} \cdot \dot{\boldsymbol{t}} + \dot{\boldsymbol{w}}^{\rm dis}$ (2.15)	$\dot{\boldsymbol{t}} = \boldsymbol{E}^{\rm d} \cdot \big(\dot{\boldsymbol{e}} - \dot{\boldsymbol{e}}^{\rm dis}\big), \quad \dot{\boldsymbol{e}} = \boldsymbol{C}^{\rm d} \cdot \dot{\boldsymbol{t}} + \dot{\boldsymbol{e}}^{\rm dis}$ (2.16)
Evolution laws	Evolution laws
$\dot{\boldsymbol{w}}^{\rm dis} = \dot{\widetilde{\boldsymbol{C}}}^{\rm d} \cdot \boldsymbol{t} + \dot{\boldsymbol{w}}^{\rm p} = \tilde{\lambda} \boldsymbol{\gamma}, \qquad \dot{\tilde{\kappa}} = \tilde{\lambda} h$ (2.17a)	$\dot{\boldsymbol{e}}^{\rm dis} = \dot{\boldsymbol{C}}^{\rm d} \cdot \boldsymbol{t} + \dot{\boldsymbol{e}}^{\rm p} = \lambda \boldsymbol{\gamma}, \qquad \dot{\kappa} = \lambda h$ (2.18a)
$\dot{\boldsymbol{w}}^{\rm p} = \big(1 - \xi\big)\, \dot{\boldsymbol{w}}^{\rm dis} = \big(1 - \xi\big)\, \tilde{\lambda} \boldsymbol{\gamma}$ (2.17b)	$\dot{\boldsymbol{e}}^{\rm p} = \big(1 - \xi\big)\, \dot{\boldsymbol{e}}^{\rm dis} = \big(1 - \xi\big)\, \lambda \boldsymbol{\gamma}$ (2.18b)
$\dot{\widetilde{\boldsymbol{C}}}^{\rm d} = \xi\, \tilde{\lambda} \dfrac{\boldsymbol{\gamma} \otimes \boldsymbol{\gamma}}{\boldsymbol{\gamma} \cdot \boldsymbol{t}}$ (2.17c)	$\dot{\boldsymbol{C}}^{\rm d} = \xi\, \lambda \dfrac{\boldsymbol{\gamma} \otimes \boldsymbol{\gamma}}{\boldsymbol{\gamma} \cdot \boldsymbol{t}}$ (2.18c)
Kuhn-Tucker loading/unloading rules	Kuhn-Tucker loading/unloading rules
$\tilde{\lambda} \geq 0, \qquad f \leq 0, \qquad \tilde{\lambda} f \equiv 0$ (2.19)	$\lambda \geq 0, \qquad f \leq 0, \qquad \lambda f \equiv 0$ (2.20)
Consistency parameter	Consistency parameter
$\tilde{\lambda} = \dfrac{\boldsymbol{\gamma} \cdot \widetilde{\boldsymbol{E}}^{\rm d} \cdot \dot{\boldsymbol{w}}}{\boldsymbol{\gamma} \cdot \widetilde{\boldsymbol{E}}^{\rm d} \cdot \boldsymbol{\gamma} + h \cdot \widetilde{H} \cdot h} = \dfrac{\boldsymbol{\gamma} \cdot \dot{\boldsymbol{t}}}{h \cdot \widetilde{H} \cdot h}$ (2.21)	$\lambda = \dfrac{\boldsymbol{\gamma} \cdot \boldsymbol{E}^{\rm d} \cdot \dot{\boldsymbol{e}}}{\boldsymbol{\gamma} \cdot \boldsymbol{E}^{\rm d} \cdot \boldsymbol{\gamma} + h \cdot H \cdot h} = \dfrac{\boldsymbol{\gamma} \cdot \dot{\boldsymbol{t}}}{h \cdot H \cdot h}$ (2.22)
Rate constitutive relations	Rate constitutive relations
$\dot{\boldsymbol{t}} = \widetilde{\boldsymbol{E}}^{\rm d}_{\rm tan} \cdot \dot{\boldsymbol{w}}, \qquad \dot{\boldsymbol{w}} = \widetilde{\boldsymbol{C}}^{\rm d}_{\rm tan} \cdot \dot{\boldsymbol{t}}$ (2.23)	$\dot{\boldsymbol{t}} = \boldsymbol{E}^{\rm d}_{\rm tan} \cdot \dot{\boldsymbol{e}}, \qquad \dot{\boldsymbol{e}} = \boldsymbol{C}^{\rm d}_{\rm tan} \cdot \dot{\boldsymbol{t}}$ (2.24a)
Discontinuity tangents	Discontinuity tangents
$\widetilde{\boldsymbol{E}}^{\rm d}_{\rm tan} = \widetilde{\boldsymbol{E}}^{\rm d} - \dfrac{\widetilde{\boldsymbol{E}}^{\rm d} \cdot \big(\boldsymbol{\gamma} \otimes \boldsymbol{\gamma}\big) \cdot \widetilde{\boldsymbol{E}}^{\rm d}}{\boldsymbol{\gamma} \cdot \widetilde{\boldsymbol{E}}^{\rm d} \cdot \boldsymbol{\gamma} + h \cdot \widetilde{H} \cdot h}$ (2.25a)	$\boldsymbol{E}^{\rm d}_{\rm tan} = \boldsymbol{E}^{\rm d} - \dfrac{\boldsymbol{E}^{\rm d} \cdot \big(\boldsymbol{\gamma} \otimes \boldsymbol{\gamma}\big) \cdot \boldsymbol{E}^{\rm d}}{\boldsymbol{\gamma} \cdot \boldsymbol{E}^{\rm d} \cdot \boldsymbol{\gamma} + h \cdot H \cdot h}$ (2.26a)
$\widetilde{\boldsymbol{C}}^{\rm d}_{\rm tan} = \widetilde{\boldsymbol{C}}^{\rm d} + \dfrac{\boldsymbol{\gamma} \otimes \boldsymbol{\gamma}}{h \cdot \widetilde{H} \cdot h}$ (2.25b)	$\boldsymbol{C}^{\rm d}_{\rm tan} = \boldsymbol{C}^{\rm d} + \dfrac{\boldsymbol{\gamma} \otimes \boldsymbol{\gamma}}{h \cdot H \cdot h}$ (2.26b)

or $\lambda = 0$. For an evolving discontinuity (band), i.e., $\tilde{\lambda} > 0$ or $\lambda > 0$, it follows that $f(\boldsymbol{t}, q) = 0$. In this case, the consistency condition $\dot{f}(\boldsymbol{t}, q) = 0$ yields the result (2.21) or (2.22), where the softening moduli are given by $\widetilde{H} := \partial q / \partial \tilde{\kappa} < 0$ and $H := \partial q / \partial \kappa < 0$, with $\tilde{\kappa}$ and κ being the displacement-like and strain-like internal variables, respectively. Owing to the associated evolution laws, the discontinuity tangents (2.25) and (2.26) are all symmetric.

2.4. *Fracture energy and the equivalence conditions*

For a strong discontinuity, the fracture energy $G_{\rm f}$, usually regarded as a material property and defined as energy dissipation W per unit of discontinuity area A_S, can be evaluated as (Wu and Cervera, 2014b)

$$G_{\rm f} := \frac{W}{A_S} = \Big(1 - \frac{1}{2}\xi\Big) \int_0^\infty \tilde{\lambda} \boldsymbol{\gamma}\ {\rm d}T = \Big(1 - \frac{1}{2}\xi\Big) \int_0^\infty q(\tilde{\kappa})\ {\rm d}\tilde{\kappa} \tag{2.28}$$

where the evolution laws (2.17) and the relation $\widehat{\boldsymbol{\gamma}} \cdot \boldsymbol{t} = \widehat{h} \cdot q$ for an active discontinuity (band) has been considered. Accordingly, the parameters involved in the softening law $q(\tilde{\kappa})$ can be determined for the given fracture energy G_{f}.

Similarly, for a regularized discontinuity it follows that

$$G_{\mathrm{f}} := \frac{W}{A_{\mathcal{S}}} = \frac{W}{V_{\mathcal{B}}/b} = b\Big(1 - \frac{1}{2}\xi\Big) \int_0^{\infty} \lambda \boldsymbol{\gamma} \, \mathrm{d}T = b\Big(1 - \frac{1}{2}\xi\Big) \int_0^{\infty} q(\kappa) \, \mathrm{d}\kappa \tag{2.29}$$

for the volume $V_{\mathcal{B}} = b A_{\mathcal{S}}$ of the discontinuity band. It can be concluded that for the given fracture energy G_{f}, the softening function $q(\kappa)$ also depends on the band width b.

The fracture energy (2.29) allows introducing the so-called specific fracture energy g_{f}, i.e., the dissipation per unit volume of the discontinuity band $V_{\mathcal{B}}$, in a straightforward manner

$$g_{\mathrm{f}} := \frac{W}{V_{\mathcal{B}}} = \frac{1}{b} G_{\mathrm{f}} \tag{2.30}$$

This is exactly the relation between the crack band theory (Bažant and Oh, 1983) and the fictitious crack model (Hillerborg et al., 1976).

For the case of a vanishing band width $b \to 0$, the relation $g_{\mathrm{f}} = G_{\mathrm{f}} \, \delta_{\mathcal{S}}$ holds. It then follows that

$$W = \int_{\mathcal{B}} g_{\mathrm{f}} \, \mathrm{d}\mathcal{B} = \int_{\mathcal{B}} G_{\mathrm{f}} \, \delta_{\mathcal{S}} \, \mathrm{d}\mathcal{B} = \int_{\mathcal{S}} G_{\mathrm{f}} \, \mathrm{d}\mathcal{S} \tag{2.31}$$

which recovers the classical definition of fracture energy.

For the same traction-based failure criterion $\widehat{f}(\boldsymbol{t}, q) \leq 0$ and equivalent softening laws $q(\kappa) = q(\tilde{\kappa})$, the results (2.28) and (2.29) imply that identical fracture energies G_{f} can be obtained for both models, provided that

$$\kappa = \frac{1}{b}\tilde{\kappa}, \qquad \dot{\kappa} = \frac{1}{b}\dot{\tilde{\kappa}} \qquad \Longleftrightarrow \qquad \lambda = \frac{1}{b}\tilde{\lambda}, \qquad \frac{1}{H} = \frac{1}{b}\frac{1}{\widetilde{H}} \tag{2.32}$$

That is, the strong discontinuity transforms into an equivalent regularized counterpart with a finite band width $b \nrightarrow 0$.

Contrariwise, for the regularized discontinuity with a vanishing band width $b \to 0$, the conditions (2.32) become

$$\kappa = \tilde{\kappa}\delta_{\mathcal{S}}, \qquad \dot{\kappa} = \dot{\tilde{\kappa}}\delta_{\mathcal{S}} \qquad \Longleftrightarrow \qquad \lambda = \tilde{\lambda}\delta_{\mathcal{S}}, \qquad \frac{1}{H} = \frac{1}{\widetilde{H}}\delta_{\mathcal{S}} \tag{2.33}$$

In this case, the regularized discontinuity localizes into an equivalent strong discontinuity.

The above results clearly show that ***the strong and regularized discontinuity approaches are consistently related***.

3. Embedded/smeared discontinuity approaches

In the above strong and regularized discontinuity approaches, the traction continuity condition $(2.1)_2$ is enforced in weak form. Alternatively, it can also be enforced point-wisely in strong form. This scheme allows elimination of the displacement jump $\boldsymbol{w}$ associated with the strong discontinuity $\mathcal{S}$ (or the inelastic deformation vector $\boldsymbol{e}$ with the regularized discontinuity $\mathcal{B}$) at the material local level. That is, the inelastic behavior caused by the strong/regularized discontinuities can be accounted for through appropriate material constitutive models, resulting in the following embedded/smeared discontinuity approaches.

3.1. Governing equations in weak form

As mentioned before, the inelastic strains $\boldsymbol{\epsilon}^{\text{in}}$ are localized completely within the discontinuity (band) and consequently, the elastic strain field $\boldsymbol{\epsilon}^{\text{e}}$ is continuous in the entire solid. It follows that, ***though the strain field may be discontinuous or even singular, the resulting stress field is continuous across the discontinuity (band)***, i.e.,

$$\boxed{\boldsymbol{\sigma}_{\mathcal{S}}^{+} = \boldsymbol{\sigma}_{\mathcal{S}}^{-} = \boldsymbol{\sigma}_{\mathcal{S}}} \tag{3.1}$$

for the stress $\boldsymbol{\sigma}_{\mathcal{S}} := \boldsymbol{\sigma}(\boldsymbol{x} \in \mathcal{S})$ at the discontinuity (band). This conclusion, applicable for both strong and regularized discontinuities, is exactly the *stress continuity condition* upon strain localization in softening solids; see Wu and Cervera (2014a,b) for the details.

In this case, the traction continuity condition $(2.1)_2$, which describes the relation between the stresses $\boldsymbol{\sigma}_{\mathcal{S}}^{+} = \boldsymbol{\sigma}_{\mathcal{S}}^{-}$ in the bulk and the cohesive traction $\boldsymbol{t}$ transferred by the discontinuity (band), coincides with the classical static constraint at the material level, i.e.,

$$\boldsymbol{t} = \boldsymbol{\sigma}_{\mathcal{S}} \cdot \boldsymbol{n}, \qquad \dot{\boldsymbol{t}} = \dot{\boldsymbol{\sigma}}_{\mathcal{S}} \cdot \boldsymbol{n} \tag{3.2}$$

where the material character of the discontinuity $\dot{\boldsymbol{n}} = \boldsymbol{0}$ has been considered. The above static constraint is employed in the embedded/smeared crack models (Rots, 1988; Armero and Oller, 1998) and traction-based elastoplastic damage models (Wu and Xu, 2011) discussed later.

With the traction continuity condition $(2.1)_2$ enforced in strong form, the governing equation $(2.1)_1$ and the traction boundary condition $(2.2)_1$ can be stated as the standard principle of virtual work: Find $\boldsymbol{u} \in \mathscr{U}$ such that

$$\int_{\Omega} \nabla^{\text{sym}} \delta\boldsymbol{u} : \boldsymbol{\sigma} \, \mathrm{d}\Omega = \int_{\Omega} \delta\boldsymbol{u} \cdot \boldsymbol{b}^{*} \, \mathrm{d}\Omega + \int_{\Gamma_t} \delta\boldsymbol{u} \cdot \boldsymbol{t}^{*} \, \mathrm{d}\Gamma \qquad \forall \delta\boldsymbol{u} \in \mathcal{V} \tag{3.3}$$

with the stress $\boldsymbol{\sigma}_{\mathcal{S}}$ at the discontinuity (band) determined from an inelastic material model satisfying the static constraint (3.2). Here, $\mathscr{U}$ is the trial space introduced in Eq. (2.5a) for a strong discontinuity or in Eq. (2.8a) for a regularized one; the standard test space $\mathcal{V}$ is defined as

$$\mathcal{V} := \left\{ \delta\boldsymbol{u} \text{ of sufficient regularity} \middle| \delta\boldsymbol{u} = \boldsymbol{0} \text{ on } \Gamma_u \right\} \tag{3.4}$$

As can be seen, the traction continuity condition $(2.1)_2$ and the displacement jump $\boldsymbol{w}$ (or the inelastic deformation vector $\boldsymbol{e}$) are not explicitly considered in the weak form (3.3). But rather, they are accounted for indirectly at the material local level, i.e., in appropriate constitutive models fulfilling the classical static constraint (3.2) for the overall weakened solid.

3.2. Embedded/smeared discontinuity models

Owing to the equivalence shown in Section 2.4, only the smeared discontinuity model employing the regularized kinematics (2.6) is addressed in the following.

As the stress field remains continuous after strain localization occurs, the constitutive relations for both the bulk and the discontinuity (band) can be expressed as

$$\boldsymbol{\sigma} = \mathbb{E}^0 : \boldsymbol{\epsilon}^{\mathrm{e}} = \mathbb{E}^0 : \big(\boldsymbol{\epsilon} - \boldsymbol{\epsilon}^{\mathrm{in}}\big), \qquad \boldsymbol{\epsilon}^{\mathrm{e}} = \boldsymbol{\epsilon} - \boldsymbol{\epsilon}^{\mathrm{in}} = \mathbb{C}^0 : \boldsymbol{\sigma} \tag{3.5}$$

or, in rate form,

$$\dot{\boldsymbol{\sigma}} = \mathbb{E}^0 : \dot{\boldsymbol{\epsilon}}^{\mathrm{e}} = \mathbb{E}^0 : \big(\dot{\boldsymbol{\epsilon}} - \dot{\boldsymbol{\epsilon}}^{\mathrm{in}}\big), \qquad \dot{\boldsymbol{\epsilon}}^{\mathrm{e}} = \dot{\boldsymbol{\epsilon}} - \dot{\boldsymbol{\epsilon}}^{\mathrm{in}} = \mathbb{C}^0 : \dot{\boldsymbol{\sigma}} \tag{3.6}$$

where the inelastic strain $\boldsymbol{\epsilon}^{\mathrm{in}}$ is defined in Eq. (2.10). Once the kinematic variable $\boldsymbol{e} := \boldsymbol{w}/b$ is eliminated through the static constraint (3.2), an inelastic material model that characterizes the overall nonlinear behavior of the solid with a regularized discontinuity is obtained.

Calling for Eqs. (2.16) and (3.6), the static constraint $(3.2)_2$ yields the following inelastic deformation vector rate $\dot{\boldsymbol{e}}$ in terms of the strain rate $\dot{\boldsymbol{\epsilon}}$

$$\dot{\boldsymbol{e}} = \big(\boldsymbol{E}_{\mathrm{tan}}^{\mathrm{d}} + \boldsymbol{n} \cdot \mathbb{E}^0 \cdot \boldsymbol{n}\big)^{-1} \cdot \big(\mathbb{E}^0 : \dot{\boldsymbol{\epsilon}}\big) \cdot \boldsymbol{n} \tag{3.7}$$

Therefore, the stress rate $\dot{\boldsymbol{\sigma}}$ is then given from Eq. (3.6), i.e.,

$$\dot{\boldsymbol{\sigma}} = \mathbb{E}^0 : \Big[\dot{\boldsymbol{\epsilon}} - \big(\dot{\boldsymbol{e}} \otimes \boldsymbol{n}\big)^{\mathrm{sym}}\Big] = \mathbb{E}_{\mathrm{tan}} : \dot{\boldsymbol{\epsilon}} \tag{3.8}$$

where the fourth-order tangent stiffness tensor $\mathbb{E}_{\mathrm{tan}}$ is expressed as

$$\mathbb{E}_{\mathrm{tan}} = \mathbb{E}^0 - \mathbb{E}^0 : \Big[\big(\boldsymbol{E}_{\mathrm{tan}}^{\mathrm{d}} + \boldsymbol{n} \cdot \mathbb{E}^0 \cdot \boldsymbol{n}\big)^{-1} \overline{\underline{\otimes}}\, \boldsymbol{N}\Big]^{\mathrm{sym}} : \mathbb{E}^0 \tag{3.9}$$

with a second-order geometric tensor $\boldsymbol{N} := \boldsymbol{n} \otimes \boldsymbol{n}$.

Alternatively, substitution of Eq. (2.24a) into the rate of the inelastic strain $(2.10)_2$ yields

$$\dot{\boldsymbol{\epsilon}}^{\mathrm{in}} = \big(\dot{\boldsymbol{e}} \otimes \boldsymbol{n}\big)^{\mathrm{sym}} = \Big[\big(\boldsymbol{C}_{\mathrm{tan}}^{\mathrm{d}} \cdot \dot{\boldsymbol{\sigma}} \cdot \boldsymbol{n}\big) \otimes \boldsymbol{n}\Big]^{\mathrm{sym}} = \big(\boldsymbol{C}_{\mathrm{tan}}^{\mathrm{d}}\, \overline{\underline{\otimes}}\, \boldsymbol{N}\big)^{\mathrm{sym}} : \dot{\boldsymbol{\sigma}} \tag{3.10}$$

where the static constraint (3.2) has been considered. The strain rate $\dot{\boldsymbol{\epsilon}}$ is then given from Eq. (2.9) as

$$\dot{\boldsymbol{\epsilon}} = \dot{\boldsymbol{\epsilon}}^{\mathrm{e}} + \dot{\boldsymbol{\epsilon}}^{\mathrm{in}} = \mathbb{C}_{\mathrm{tan}} : \dot{\boldsymbol{\sigma}} \tag{3.11}$$

where the fourth-order tangent compliance tensor $\mathbb{C}_{\mathrm{tan}}$ is expressed as

$$\mathbb{C}_{\mathrm{tan}} = \mathbb{C}^0 + \big(\boldsymbol{C}_{\mathrm{tan}}^{\mathrm{d}}\, \overline{\underline{\otimes}}\, \boldsymbol{N}\big)^{\mathrm{sym}} \tag{3.12}$$

Note that the above tangent compliance tensor $\mathbb{C}_{\mathrm{tan}}$ can also be directly derived from Eq. (3.9) through the Sherman-Morrison-Woodburg formula (Golub and van Loan, 1996).

The above constitutive relations correspond exactly to those in the smeared crack model (Rots, 1985, 1988; Rots and Blaauwendraad, 1989), as an extension of the original form proposed by Rashid (1968).

3.3. Traction-based elastoplastic degradation model

As shown in Eqs. (2.11)$_2$ and (2.12)$_2$, the strain (2.9) in the discontinuity (band) is decomposed into its elastic, damage and plastic parts. This kinematic decomposition, depicted in Fig. 6, is exactly the one advocated by Armero and Oller (1998). The resulting embedded/smeared discontinuity models then fit the framework developed in that reference. In this section it is shown that they can be cast into an alternative framework with a different kinematic decomposition.

Calling for the constitutive relation (2.14) and the static constraint (3.2), the damage strain $\boldsymbol{\epsilon}^{\mathrm{d}}$ can be explicitly related to the stress tensor $\boldsymbol{\sigma}$

$$\boldsymbol{\epsilon}^{\mathrm{d}} = \Big[\big(\boldsymbol{C}^{\mathrm{d}} \cdot \boldsymbol{\sigma} \cdot \boldsymbol{n}\big) \otimes \boldsymbol{n}\Big]^{\mathrm{sym}} = \mathbb{C}^{\mathrm{d}} : \boldsymbol{\sigma} \tag{3.13}$$

where the symmetric fourth-order damage compliance tensor $\mathbb{C}^{\mathrm{d}}$ is expressed as

$$\mathbb{C}^{\mathrm{d}} = \big(\boldsymbol{C}^{\mathrm{d}} \overline{\underline{\otimes}} \boldsymbol{N}\big)^{\mathrm{sym}} \tag{3.14}$$

Accordingly, the strain $\boldsymbol{\epsilon}$ in Eq. (2.9) can be decomposed into a recoverable (elastic and damage) part $\mathbb{C} : \boldsymbol{\sigma} = \boldsymbol{\epsilon}^{\mathrm{e}} + \boldsymbol{\epsilon}^{\mathrm{d}}$ and an irreversible plastic one $\boldsymbol{\epsilon}^{\mathrm{p}}$.

$$\boldsymbol{\epsilon} = \boldsymbol{\epsilon}^{\mathrm{e}} + \boldsymbol{\epsilon}^{\mathrm{d}} + \boldsymbol{\epsilon}^{\mathrm{p}} = \mathbb{C}^0 : \boldsymbol{\sigma} + \mathbb{C}^{\mathrm{d}} : \boldsymbol{\sigma} + \boldsymbol{\epsilon}^{\mathrm{p}} = \mathbb{C} : \boldsymbol{\sigma} + \boldsymbol{\epsilon}^{\mathrm{p}} \tag{3.15}$$

where the fourth-order compliance tensor $\mathbb{C}$ is given by

$$\mathbb{C} := \mathbb{C}^0 + \mathbb{C}^{\mathrm{d}} = \mathbb{C}^0 + \big(\boldsymbol{C}^{\mathrm{d}} \overline{\underline{\otimes}} \boldsymbol{N}\big)^{\mathrm{sym}} \tag{3.16}$$

This is the kinematic decomposition employed in the so-called elastoplastic degradation framework (Ortiz, 1985; Meschke et al., 1998; Wu and Xu, 2011); also see Fig. 6.

Inversely, the stress rate $\boldsymbol{\sigma}$ is then evaluated as

$$\boldsymbol{\sigma} = \mathbb{E} : \big(\boldsymbol{\epsilon} - \boldsymbol{\epsilon}^{\mathrm{p}}\big) \tag{3.17}$$

where the fourth-order stiffness tensor $\mathbb{E} = \mathbb{C}^{-1}$ is obtained from the Sherman-Morrison-Woodburg formula (Golub and van Loan, 1996), i.e.,

$$\mathbb{E} = \mathbb{E}^0 - \mathbb{E}^0 : \Big[\big(\boldsymbol{E}^{\mathrm{d}} + \boldsymbol{n} \cdot \mathbb{E}^0 \cdot \boldsymbol{n}\big)^{-1} \overline{\underline{\otimes}} \boldsymbol{N}\Big]^{\mathrm{sym}} : \mathbb{E}^0 \tag{3.18}$$

It is important to note that, due to the rank deficiency of the fourth-order damage compliance tensor $\mathbb{C}^{\mathrm{d}}$, Eq. (3.13) in general can not be inverted to determine the stress $\boldsymbol{\sigma}$ solely from the damage strain $\boldsymbol{\epsilon}^{\mathrm{d}}$.

It follows from the evolution laws (2.18) that

$$\dot{\boldsymbol{\epsilon}}^{\mathrm{p}} = \big(\dot{\boldsymbol{e}}^{\mathrm{p}} \otimes \boldsymbol{n}\big)^{\mathrm{sym}} = \big(1 - \xi\big)\, \lambda \boldsymbol{\Lambda} \tag{3.19a}$$

$$\dot{\mathbb{C}} = \dot{\mathbb{C}}^{\mathrm{d}} = \big(\dot{\boldsymbol{C}}^{\mathrm{d}} \overline{\underline{\otimes}} \boldsymbol{N}\big)^{\mathrm{sym}} = \xi\, \lambda \frac{\boldsymbol{\Lambda} \otimes \boldsymbol{\Lambda}}{\boldsymbol{\Lambda} : \boldsymbol{\sigma}} \tag{3.19b}$$

where the following definition of the dissipative flow tensor $\boldsymbol{\Lambda}$ has been introduced

$$\boldsymbol{\Lambda} := \big(\boldsymbol{\gamma} \otimes \boldsymbol{n}\big)^{\text{sym}}, \qquad \boldsymbol{\gamma} := \frac{\partial f}{\partial \boldsymbol{t}} \tag{3.20a}$$

Owing to the static constraint (3.2), the above dissipative flow tensor $\boldsymbol{\Lambda}$ can also be expressed as

$$\boldsymbol{\Lambda} = \frac{\partial f}{\partial \boldsymbol{\sigma}} = \boldsymbol{\mathcal{N}} \cdot \boldsymbol{\gamma} = \big(\boldsymbol{\gamma} \otimes \boldsymbol{n}\big)^{\text{sym}} \tag{3.20b}$$

where $\boldsymbol{\mathcal{N}} = \partial \boldsymbol{t} / \partial \boldsymbol{\sigma}$ is a third-order tensor with components $\mathcal{N}_{ijk} = \frac{1}{2}\big(n_i \delta_{jk} + n_j \delta_{ik}\big)$, for the Cartesian components n_i of the normal vector $\boldsymbol{n}$ and the Kronecker-delta δ_{jk}, respectively.

By time differentiation, the strain rate $\dot{\boldsymbol{\epsilon}}$ and the stress rate $\dot{\boldsymbol{\sigma}}$ are expressed as

$$\dot{\boldsymbol{\epsilon}} = \mathbb{C} : \dot{\boldsymbol{\sigma}} + \dot{\boldsymbol{\epsilon}}^{\text{dis}}, \qquad \dot{\boldsymbol{\sigma}} = \mathbb{E} : \big(\dot{\boldsymbol{\epsilon}} - \dot{\boldsymbol{\epsilon}}^{\text{dis}}\big) \tag{3.21}$$

where the *dissipative strain tensor rate* $\dot{\boldsymbol{\epsilon}}^{\text{dis}}$ (Wu and Xu, 2013), related to the energy dissipation, is defined as

$$\dot{\boldsymbol{\epsilon}}^{\text{dis}} := \dot{\mathbb{C}}^{\text{d}} : \boldsymbol{\sigma} + \dot{\boldsymbol{\epsilon}}^{\text{p}} = \big(\dot{\boldsymbol{e}}^{\text{dis}} \otimes \boldsymbol{n}\big)^{\text{sym}} = \lambda \boldsymbol{\Lambda} \tag{3.22}$$

with $\dot{\mathbb{C}}^{\text{d}} : \boldsymbol{\sigma}$ and $\dot{\boldsymbol{\epsilon}}^{\text{p}}$ being its damage and plastic components, respectively; see Fig. 7 for the 1D illustration. Note that the so-called degradation strain rate $\dot{\mathbb{C}}^{\text{d}} : \boldsymbol{\sigma}$ (Dougill, 1976; Hueckel and Maier, 1977; Carol et al., 1994) and the dissipative strain rate $\dot{\boldsymbol{\epsilon}}^{\text{dis}}$ are meaningful only in rate sense.

For the traction-based failure criterion (2.27), the Lagrangian multiplier $\lambda > 0$ is solved from the consistency condition $\dot{f} = 0$ as

$$\lambda = \frac{\boldsymbol{\Lambda} : \mathbb{E} : \dot{\boldsymbol{\epsilon}}}{\boldsymbol{\Lambda} : \mathbb{E} : \boldsymbol{\Lambda} + h \cdot H \cdot h} = \frac{\boldsymbol{\Lambda} : \dot{\boldsymbol{\sigma}}}{h \cdot H \cdot h} \tag{3.23}$$

Note that the above Lagrangian multiplier λ is expressed in terms of the strain rate $\dot{\boldsymbol{\epsilon}}$, rather than the rate of the kinematic unknowns $\dot{\boldsymbol{w}}$ (or $\dot{\boldsymbol{e}}$) as in the cohesive constitutive models for strong/regularized discontinuities; see Eq. (2.21) or (2.22).

Therefore, the following rate constitutive relations are obtained

$$\dot{\boldsymbol{\sigma}} = \mathbb{E} : \big(\dot{\boldsymbol{\epsilon}} - \lambda \boldsymbol{\Lambda}\big) = \mathbb{E}_{\text{tan}} : \dot{\boldsymbol{\epsilon}} \tag{3.24a}$$

$$\dot{\boldsymbol{\epsilon}} = \mathbb{C} : \dot{\boldsymbol{\sigma}} + \lambda \boldsymbol{\Lambda} = \mathbb{C}_{\text{tan}} : \dot{\boldsymbol{\sigma}} \tag{3.24b}$$

where the symmetric material tangents $\mathbb{E}_{\text{tan}}$ and $\mathbb{C}_{\text{tan}}$ are expressed as

$$\mathbb{E}_{\text{tan}} = \mathbb{E} - \frac{\mathbb{E} : \big(\boldsymbol{\Lambda} \otimes \boldsymbol{\Lambda}\big) : \mathbb{E}}{\boldsymbol{\Lambda} : \mathbb{E} : \boldsymbol{\Lambda} + h \cdot H \cdot h} \tag{3.25a}$$

$$\mathbb{C}_{\text{tan}} = \mathbb{C} + \frac{\boldsymbol{\Lambda} \otimes \boldsymbol{\Lambda}}{h \cdot H \cdot h} \tag{3.25b}$$

Using the Sherman-Morrison-Woodburg formula (Golub and van Loan, 1996), it can be proved that the tangent stiffness tensors $\mathbb{E}^{\text{tan}}$ obtained in Eqs. (3.9) and (3.25a) are identical; see Appendix A for the details. Calling for the material compliance (3.16) and the relation (3.20), it can be also concluded that the tangent compliance tensors $\mathbb{C}^{\text{tan}}$ given in Eqs. (3.12) and (3.25b) coincide. Therefore, the traction-based elastoplastic degradation model is equivalent to the embedded/smeared discontinuity models.

4. Determination of the discontinuity orientation

In both the strong/regularized discontinuity approaches and their embedded/smeared counterparts, the inelastic behavior of the discontinuity (band) is characterized by a failure criterion $f(\boldsymbol{t}, q) \leq 0$ in terms of the traction $\boldsymbol{t} = \boldsymbol{\sigma} \cdot \boldsymbol{n}$. Accordingly, the orientation $\boldsymbol{n}$ of the discontinuity (band) has to be determined.

4.1. Characteristic angles of the discontinuity

To characterize the discontinuity orientation $\boldsymbol{n}$, let us consider the spectral decomposition of the stress tensor $\boldsymbol{\sigma}$

$$\boldsymbol{\sigma} = \sum_{i=1}^{3} \sigma_i \boldsymbol{v}_i \otimes \boldsymbol{v}_i \tag{4.1}$$

where σ_i denotes the i-th principal value of the stress tensor $\boldsymbol{\sigma}$, with the corresponding principal vectors $\boldsymbol{v}_i$ satisfying the orthogonal property $\boldsymbol{v}_i \cdot \boldsymbol{v}_j = \delta_{ij}$ for $i, j = 1, 2, 3$.

For general 3D cases, a local orthogonal base $(\boldsymbol{n}, \boldsymbol{m}, \boldsymbol{p})$ is introduced, with vectors $\boldsymbol{m}$ and $\boldsymbol{p}$ perpendicular to the normal vector $\boldsymbol{n}$ and tangent to the discontinuity surface $\mathcal{S}$. In the coordinate system of the principal stresses, the base vectors $(\boldsymbol{n}, \boldsymbol{m}, \boldsymbol{p})$ of the discontinuity can be expressed as

$$\boldsymbol{n}(\boldsymbol{\theta}) = \big\{\sin\vartheta_1 \cos\theta_1,\ \sin\vartheta_1 \sin\theta_1,\ \cos\vartheta_1\big\}^{\mathrm{T}} \tag{4.2a}$$

$$\boldsymbol{m}(\boldsymbol{\theta}) = \big\{\sin\vartheta_2 \cos\theta_2,\ \sin\vartheta_2 \sin\theta_2,\ \cos\vartheta_2\big\}^{\mathrm{T}} \tag{4.2b}$$

$$\boldsymbol{p}(\boldsymbol{\theta}) = \boldsymbol{n}(\boldsymbol{\theta}) \times \boldsymbol{m}(\boldsymbol{\theta}) \tag{4.2c}$$

supplemented with an additional equation resulting from the orthogonality $\boldsymbol{n} \cdot \boldsymbol{m} = 0$

$$C(\boldsymbol{\theta}) := \boldsymbol{n}(\boldsymbol{\theta}) \cdot \boldsymbol{m}(\boldsymbol{\theta}) = \sin\vartheta_1 \sin\vartheta_2 \cos\big(\theta_1 - \theta_2\big) + \cos\vartheta_1 \cos\vartheta_2 = 0 \tag{4.2d}$$

where $\boldsymbol{\theta} := \big\{\theta_1, \theta_2, \vartheta_1, \vartheta_2\big\}^{\mathrm{T}}$ is a set of characteristic angles, with (θ_1, θ_2) and $(\vartheta_1, \vartheta_2)$ being the spherical azimuth and polar angles, respectively; the operator "×" denotes the Gibbs' vector product (the right hand rule is followed). In this way, the discontinuity orientation $\boldsymbol{n}$ can be characterized by a specific set of discontinuity angles $\boldsymbol{\theta}^{\mathrm{cr}}$.

The tractions $\boldsymbol{t}$ acting on the surface with normal vector $\boldsymbol{n}(\boldsymbol{\theta})$ are given by

$$\boldsymbol{t} := \boldsymbol{\sigma} \cdot \boldsymbol{n} = t_n \boldsymbol{n} + t_m \boldsymbol{m} + t_p \boldsymbol{p} \tag{4.3}$$

for the following traction components (t_n, t_m, t_p)

$$t_n = \sigma_{nn} = \boldsymbol{n} \cdot \boldsymbol{t} = \big(\boldsymbol{n} \otimes \boldsymbol{n}\big) : \boldsymbol{\sigma} \tag{4.4a}$$

$$t_m = \sigma_{nm} = \boldsymbol{m} \cdot \boldsymbol{t} = \big(\boldsymbol{n} \otimes \boldsymbol{m}\big)^{\mathrm{sym}} : \boldsymbol{\sigma} \tag{4.4b}$$

$$t_p = \sigma_{np} = \boldsymbol{p} \cdot \boldsymbol{t} = \big(\boldsymbol{n} \otimes \boldsymbol{p}\big)^{\mathrm{sym}} : \boldsymbol{\sigma} \tag{4.4c}$$

That is, the traction components (t_n, t_m, t_p) can also be related to the characteristic angles $\boldsymbol{\theta}$.

4.2. *Morh's maximization postulate*

It is a non-trivial goal to determine the discontinuity orientation for a new or propagating discontinuity. As mentioned before, the occurrence of necessary requirements for a certain type of failure (e.g., discontinuous bifurcation) to be initiated during the deformation process in inelastic solids provides useful information about the discontinuity orientation; see (Runesson et al., 1991; Ottosen and Runesson, 1991a) and the references therein. Recently, in oder to guarantee formation of localization band in softening materials and its eventual evolution into a fully softened discontinuity, the authors proposed a novel strain localization analysis based on a more stringent stress continuity condition (Wu and Cervera, 2014a,b). Particularly, for a softening solid with its inelastic behavior characterized by a given dissipative flow tensor $\boldsymbol{\Lambda} = \partial F / \partial \boldsymbol{\sigma}$, with $F(\boldsymbol{\sigma}, q) \leq 0$ being a stress-based failure criterion, a kinematic constraint of identical form (3.20) fulfilling stress continuity (3.1) upon strain localization is derived. It is proved that in the case of associated evolution laws, the stress continuity based kinematic constraint is equivalent to Mohr's maximization postulate (Mohr, 1900), provided the stress-based failure criterion and the traction-based counterpart are *conformityously* related. This fact justifies the use of Mohr's maximization postulate for the determination of discontinuity orientation in the case of associated evolution laws.

For the case considered here, provided strain localization with a continuous stress field can occur, the traction-based failure criterion (2.27) can always be obtained by projecting the corresponding stress-based one $F(\boldsymbol{\sigma}, q) \leq 0$

$$F(\boldsymbol{\sigma}, q) := f(\boldsymbol{t}, q) = \frac{1}{M}\big(\boldsymbol{\gamma} \cdot \boldsymbol{t} - h \cdot q\big) = \frac{1}{M}\big(\boldsymbol{\Lambda} : \boldsymbol{\sigma} - h \cdot q\big) \leq 0 \tag{4.5}$$

onto the discontinuity orientation, where the following identity has been considered

$$\boldsymbol{\Lambda} := \big(\boldsymbol{\gamma} \otimes \boldsymbol{n}\big)^{\text{sym}} \qquad \Longrightarrow \qquad \boldsymbol{\Lambda} : \boldsymbol{\sigma} = \boldsymbol{\gamma} \cdot \boldsymbol{t} \tag{4.6}$$

for the dissipative flow tensor defined in Eq. (3.20). Accordingly, for the discontinuity (band) to form along the orientation $\boldsymbol{n}(\boldsymbol{\theta}^{\text{cr}})$, the traction-based failure criterion $f(\boldsymbol{t}, q) = 0$ is activated. Meanwhile, no discontinuity (band) forms at any other orientation $\boldsymbol{n}(\boldsymbol{\theta}) \neq \boldsymbol{n}(\boldsymbol{\theta}^{\text{cr}})$. Calling for the static constraint (3.2), the above facts exactly transform into Mohr's maximum postulate

$$f\big[\boldsymbol{\sigma} \cdot \boldsymbol{n}(\boldsymbol{\theta}), q\big] \leq f\big[\boldsymbol{\sigma} \cdot \boldsymbol{n}(\boldsymbol{\theta}^{\text{cr}}), q\big] = 0 \tag{4.7}$$

That is, the inelastic behavior characterized by the stress-based failure criterion (4.5) is completely restricted into a discontinuity described by the traction-based counterpart (2.27) along the orientation $\boldsymbol{n}(\boldsymbol{\theta}^{\text{cr}})$ determined from Mohr's maximization postulate, i.e.,

$$\boldsymbol{\theta}^{\text{cr}} = \arg\max f\big[\boldsymbol{t}(\boldsymbol{\theta}), q\big] = \arg\max f\big[\boldsymbol{\sigma} \cdot \boldsymbol{n}(\boldsymbol{\theta}), q\big] \tag{4.8}$$

The corresponding stationarity condition reads

$$\left.\frac{\partial f}{\partial \boldsymbol{\theta}}\right|_{\boldsymbol{\theta}^{\text{cr}}} = \left(\boldsymbol{\gamma} \cdot \frac{\partial \boldsymbol{t}}{\partial \boldsymbol{\theta}}\right)_{\boldsymbol{\theta}^{\text{cr}}} = \left(\gamma_n \frac{\partial t_n}{\partial \boldsymbol{\theta}} + \gamma_m \frac{\partial t_m}{\partial \boldsymbol{\theta}} + \gamma_p \frac{\partial t_p}{\partial \boldsymbol{\theta}}\right)_{\boldsymbol{\theta}^{\text{cr}}} = \boldsymbol{0} \tag{4.9}$$

together with a negative definite Hessian matrix

$$\boldsymbol{\theta}^* \cdot \left. \frac{\partial^2 f}{\partial \boldsymbol{\theta}^2} \right|_{\boldsymbol{\theta}^{\mathrm{cr}}} \cdot \boldsymbol{\theta}^* < 0 \qquad \forall \boldsymbol{\theta}^* \tag{4.10}$$

where the dissipative flow vector $\boldsymbol{\gamma} := \partial f / \partial \boldsymbol{t}$ is expressed as

$$\boldsymbol{\gamma} = \gamma_n \boldsymbol{n} + \gamma_m \boldsymbol{m} + \gamma_p \boldsymbol{p} \tag{4.11}$$

for the following local Cartesian components

$$\gamma_n = \boldsymbol{\gamma} \cdot \boldsymbol{n} = \frac{\partial f}{\partial t_n}, \qquad \gamma_m = \boldsymbol{\gamma} \cdot \boldsymbol{m} = \frac{\partial f}{\partial t_m}, \qquad \gamma_p = \boldsymbol{\gamma} \cdot \boldsymbol{p} = \frac{\partial f}{\partial t_p} \tag{4.12}$$

Recalling the traction components (4.4), the stationarity condition (4.9) results in a set of nonlinear equations from which generally two values of the discontinuity angles $\boldsymbol{\theta}^{\mathrm{cr}}$ can be solved. Note that, provided the solution exists, it depends only on the given traction-based failure criterion and the stress state.

Remark 4.1 In the determination of the discontinuity angles $\boldsymbol{\theta}^{\mathrm{cr}}$ under general 3D cases, the constraint (4.2d) can be readily handled by the Lagrangian multiplier method. □

4.3. Closed-form results in plane stress conditions

In this section the general 3D results presented in previous sections are particularized to the plane stress conditions ($\sigma_3 = 0$). The plane strain results are discussed in Wu and Cervera (2014b).

Let us consider the 2D plane stress solid $\Omega \subset \mathbb{R}^2$ shown in Fig. 8. The unit normal vector $\boldsymbol{n}$ and tangential vector $\boldsymbol{m}$ of the discontinuity $\mathcal{S}$ are on the plane of interest. Let $\theta \in [-\pi/2, \pi/2]$ denote the angle (anti-clockwise) between the normal vector $\boldsymbol{n}$ and major principal vector $\boldsymbol{v}_1$ of the stress $\boldsymbol{\sigma}$. Accordingly, in the characteristic angles $\boldsymbol{\theta} := \{\theta_1, \theta_2, \vartheta_1, \vartheta_2\}^{\mathrm{T}}$ the azimuth angles are $\theta_1 = \theta$ and $\theta_2 = \theta - \pi/2$, and the polar angles are $\vartheta_1 = \vartheta_2 = \pi/2$. It follows that $\boldsymbol{n} = \{\cos\theta, \sin\theta, 0\}^{\mathrm{T}}$, $\boldsymbol{m} = \{\sin\theta, -\cos\theta, 0\}^{\mathrm{T}}$ and the other tangential vector $\boldsymbol{p} = \{0, 0, -1\}^{\mathrm{T}}$.

The in-plane stress components $(\sigma_{nn}, \sigma_{mm}, \sigma_{nm})$ are given from Eqs. (4.4)

$$\sigma_{nn} = \sigma_1 \cos^2\theta + \sigma_2 \sin^2\theta = \frac{\sigma_1 + \sigma_2}{2} + \frac{\sigma_1 - \sigma_2}{2} \cos(2\theta) \tag{4.13a}$$

$$\sigma_{mm} = \sigma_1 \sin^2\theta + \sigma_2 \cos^2\theta = \frac{\sigma_1 + \sigma_2}{2} - \frac{\sigma_1 - \sigma_2}{2} \cos(2\theta) \tag{4.13b}$$

$$\sigma_{nm} = (\sigma_1 - \sigma_2) \sin\theta \cos\theta = \frac{\sigma_1 - \sigma_2}{2} \sin(2\theta) \tag{4.13c}$$

with σ_1 and σ_2 being the in-plane principal stresses, ordered as $\sigma_1 \geq \sigma_2$.

As the dissipative flow tensor $\boldsymbol{\Lambda}$ is coaxial to the stress $\boldsymbol{\sigma}$ (Itskov, 2007), its in-plane components $(\Lambda_{nn}, \Lambda_{mm}, \Lambda_{nm})$ is similarly given by

$$\Lambda_{nn} = \Lambda_1 \cos^2\theta + \Lambda_2 \sin^2\theta = \frac{\Lambda_1 + \Lambda_2}{2} + \frac{\Lambda_1 - \Lambda_2}{2} \cos(2\theta) \tag{4.14a}$$

$$\Lambda_{mm} = \Lambda_1 \sin^2\theta + \Lambda_2 \cos^2\theta = \frac{\Lambda_1 + \Lambda_2}{2} - \frac{\Lambda_1 - \Lambda_2}{2} \cos(2\theta) \tag{4.14b}$$

$$\Lambda_{nm} = (\Lambda_1 - \Lambda_2) \cos\theta \sin\theta = \frac{\Lambda_1 - \Lambda_2}{2} \sin(2\theta) \tag{4.14c}$$

for the in-plane principal values Λ_1 and Λ_2. The relation $\Lambda_1 \geq \Lambda_2$ is assumed so that the identity $\mathrm{sign}(\Lambda_{nm}) = \mathrm{sign}(\sigma_{nm})$ holds, with $\mathrm{sign}(\cdot)$ being the sign function.

Note that in the plane stress condition all the out-of-plane components of tensors $\boldsymbol{\sigma}$ and $\boldsymbol{\Lambda}$ vanish, i.e., $\sigma_{pp} = \sigma_{np} = \sigma_{mp} = 0$ and $\Lambda_{pp} = \Lambda_{np} = \Lambda_{mp} = 0$.

4.3.1. Discontinuity angle

For a given plane stress traction-based failure criterion $f(\boldsymbol{t}, q) := f(t_n, t_m; q) \leq 0$, the stationarity condition (4.9) simplifies as

$$\frac{\partial f}{\partial \theta}\bigg|_{\theta^{\mathrm{cr}}} = \left(\gamma_n \frac{\partial t_n}{\partial \theta} + \gamma_m \frac{\partial t_m}{\partial \theta}\right)_{\theta^{\mathrm{cr}}} = -\big(\sigma_1 - \sigma_2\big)\Big[\gamma_n \sin(2\theta^{\mathrm{cr}}) - \gamma_m \cos(2\theta^{\mathrm{cr}})\Big] = 0 \tag{4.15}$$

The discontinuity angle θ^{cr} is then determined implicitly from

$$\tan(2\theta^{\mathrm{cr}}) = \frac{\sin(2\theta^{\mathrm{cr}})}{\cos(2\theta^{\mathrm{cr}})} = \frac{\gamma_m}{\gamma_n} \tag{4.16}$$

which should also satisfy the following maximum condition

$$\frac{\partial^2 f}{\partial \theta^2}\bigg|_{\theta^{\mathrm{cr}}} < 0 \tag{4.17}$$

Dependent on the specific stress state, two values of the discontinuity angle θ^{cr} can be obtained from Eqs. (4.16) and (4.17).

Alternatively, the discontinuity angle θ^{cr} can be expressed in terms of the dissipative flow tensor $\boldsymbol{\Lambda}$. It follows from the definition (3.20) that

$$\Lambda_{nn} = \gamma_n, \qquad \Lambda_{nm} = \frac{1}{2}\gamma_m \tag{4.18}$$

Substitution of the relations (4.14) and (4.18) into the stationarity condition (4.15) yields

$$\frac{\partial f}{\partial \theta}\bigg|_{\theta^{\mathrm{cr}}} = -\big(\sigma_1 - \sigma_2\big)\left[\frac{\Lambda_1 + \Lambda_2}{2} - \frac{\Lambda_1 - \Lambda_2}{2}\cos(2\theta^{\mathrm{cr}})\right]\sin(2\theta^{\mathrm{cr}}) = 0 \tag{4.19}$$

Furthermore, the maximization condition (4.17) requires

$$\frac{\partial^2 f}{\partial \theta^2}\bigg|_{\theta^{\mathrm{cr}}} = -\big(\sigma_1 - \sigma_2\big)\left[\big(\Lambda_1 + \Lambda_2\big)\cos(2\theta^{\mathrm{cr}}) - \big(\Lambda_1 - \Lambda_2\big)\cos(4\theta^{\mathrm{cr}})\right] < 0 \tag{4.20}$$

Therefore, the discontinuity angle θ^{cr} is identified from

$$\cos(2\theta^{\mathrm{cr}}) = \frac{\Lambda_1 + \Lambda_2}{\Lambda_1 - \Lambda_2}, \qquad \sin(2\theta^{\mathrm{cr}}) = 2\mathrm{sign}(\Lambda_{nm})\frac{\sqrt{-\Lambda_1 \Lambda_2}}{\Lambda_1 - \Lambda_2} \tag{4.21a}$$

or, equivalently,

$$\cos^2\theta^{\mathrm{cr}} = \frac{\Lambda_1}{\Lambda_1 - \Lambda_2}, \qquad \sin^2\theta^{\mathrm{cr}} = -\frac{\Lambda_2}{\Lambda_1 - \Lambda_2} \tag{4.21b}$$

if the conditions $\mathit{\Lambda}_1 \geq 0$ and $\mathit{\Lambda}_2 \leq 0$ are satisfied. For the cases $\mathit{\Lambda}_2 > 0$ or $\mathit{\Lambda}_1 < 0$, the following results apply

$$\sin(2\theta^{\mathrm{cr}}) = 0 \qquad \Longrightarrow \qquad \begin{cases} \theta^{\mathrm{cr}} = 0 & \mathit{\Lambda}_1 \geq \mathit{\Lambda}_2 > 0 \\ \theta^{\mathrm{cr}} = \pi/2 & \mathit{\Lambda}_2 \leq \mathit{\Lambda}_1 < 0 \end{cases} \tag{4.22}$$

In such cases, the traction-based failure function $f(\boldsymbol{t}, q)$ becomes

$$f(\boldsymbol{t}, q) = \begin{cases} \dfrac{1}{M}\Big[\Big(\gamma_n\big|_{\mathit{\Lambda}_2=0}\Big)t_n - h \cdot q\Big] & \mathit{\Lambda}_1 > \mathit{\Lambda}_2 > 0 \\ \dfrac{1}{M}\Big[\Big(\gamma_n\big|_{\mathit{\Lambda}_1=0}\Big)t_n - h \cdot q\Big] & \mathit{\Lambda}_2 < \mathit{\Lambda}_2 < 0 \end{cases} \tag{4.23}$$

That is, the tangential traction t_m is removed from the traction-based failure criterion.

Remark 4.2 For the discontinuity angle θ^{cr} determined from Eq. (4.21) or (4.22), it follows that $\mathit{\Lambda}_{mm}(\theta^{\mathrm{cr}}) = 0$. The above result is exactly the kinematic constraint guaranteeing stress continuity upon strain localization in plane stress conditions. □

Remark 4.3 In the plane stress condition with associated evolution laws, the results obtained from the conditions for the loss of material ellipticity, Mohr's maximization postulate and the novel stress boundedness/continuity based localization analysis, all coincide. However, this conclusion cannot be extended to other cases such as plane strain condition or non-associated evolution laws. Furthermore, only the stress boundedness/continuity based localization analysis provides a systematical approach to derive conformityent traction- and stress-based failure criteria in general cases; see Wu and Cervera (2014b) for the details.

4.3.2. Stress-based failure criterion

For the discontinuity angle θ^{cr} determined from Eq. (4.21), the normal and tangential dissipative flow components (γ_n, γ_m) are given by

$$\gamma_n = \mathit{\Lambda}_{nn}(\theta^{\mathrm{cr}}) = \mathit{\Lambda}_1 + \mathit{\Lambda}_2, \qquad \gamma_m = 2\mathit{\Lambda}_{nm}(\theta^{\mathrm{cr}}) = 2\mathrm{sign}(t_m)\,\sqrt{-\mathit{\Lambda}_1\mathit{\Lambda}_2} \tag{4.24}$$

Similarly, the normal and tangential tractions (t_n, t_m) are expressed as

$$t_n = \sigma_{nn} = \frac{\mathit{\Lambda}_1\sigma_1 - \mathit{\Lambda}_2\sigma_2}{\mathit{\Lambda}_1 - \mathit{\Lambda}_2} \tag{4.25a}$$

$$t_m = \sigma_{nm} = \mathrm{sign}(t_m)\big(\sigma_1 - \sigma_2\big)\frac{\sqrt{-\mathit{\Lambda}_1\mathit{\Lambda}_2}}{\mathit{\Lambda}_1 - \mathit{\Lambda}_2} \tag{4.25b}$$

Accordingly, the identity (4.5) is recovered, i.e.,

$$\boldsymbol{\gamma} \cdot \boldsymbol{t} = \gamma_n t_n + \gamma_m t_m = \mathit{\Lambda}_1\sigma_1 + \mathit{\Lambda}_2\sigma_2 = \boldsymbol{\mathit{\Lambda}} : \boldsymbol{\sigma} \tag{4.26}$$

so that the stress-based failure criterion $F(\boldsymbol{\sigma}, q) \leq 0$ is given from Eq. (4.5)

$$F(\boldsymbol{\sigma}, q) = \frac{1}{M}\Big[\big(\mathit{\Lambda}_1\sigma_1 + \mathit{\Lambda}_2\sigma_2\big) - h \cdot q\Big] \leq 0 \tag{4.27}$$

Note that for the cases $\Lambda_2 > 0$ or $\Lambda_1 < 0$, the stress-based failure function $F(\boldsymbol{\sigma}, q)$ corresponding to the traction-based counterpart (4.23) becomes

$$F(\boldsymbol{\sigma}, q) = \begin{cases} \dfrac{1}{M}\Big[\Big(\Lambda_1\big|_{\Lambda_2=0}\Big)\sigma_1 - h \cdot q\Big] & \Lambda_1 > \Lambda_2 > 0 \\ \dfrac{1}{M}\Big[\Big(\Lambda_2\big|_{\Lambda_1=0}\Big)\sigma_2 - h \cdot q\Big] & \Lambda_2 < \Lambda_1 < 0 \end{cases} \tag{4.28}$$

This is equivalent to introducing tension- and compression-extensions into the stress-based failure criterion (4.27).

4.4. *Prototype examples*

In this section several traction-based failure criteria corresponding to the classical Rankine, Mohr-Coulomb, von Mises and Drucker-Prager models are exemplified.

4.4.1. *Rankine criterion*

Let us first consider the following traction-based failure criterion for a pure mode-I discontinuity

$$f(\boldsymbol{t}, q) = \langle t_n \rangle - q = \mathscr{H}(t_n)\, t_n - q \leq 0 \tag{4.29}$$

where the Macaulay brackets $\langle \cdot \rangle$ and Heaviside function $\mathscr{H}(\cdot)$ are defined as: $\langle x \rangle = x$, $\mathscr{H}(x) = 1$ if $x > 0$, and $\langle x \rangle = 0$, $\mathscr{H}(x) = 0$ otherwise, respectively.

The stationarity condition (4.15) gives

$$\sin\left(2\theta^{\mathrm{cr}}\right) = 0 \qquad \Longrightarrow \qquad \theta^{\mathrm{cr}} = 0 \tag{4.30}$$

Note that in this case a unique value is obtained for θ^{cr}. With the above discontinuity angle, it follows from Eq. (4.13) that

$$t_n = \sigma_1, \qquad t_m = 0 \tag{4.31}$$

Accordingly, the traction-based failure criterion (4.29) is rewritten as the classical Rankine model

$$F(\boldsymbol{\sigma}, q) = \langle \sigma_1 \rangle - q \leq 0 \tag{4.32}$$

for the major principal stress $\sigma_1 = \boldsymbol{v}_1 \cdot \boldsymbol{\sigma} \cdot \boldsymbol{v}_1 > 0$.

4.4.2. *Mohr-Coulomb criterion*

The traction-based Mohr-Coulomb criterion is expressed as

$$f(\boldsymbol{t}, q) = \tan\varphi \cdot t_n + \left|t_m\right| - q \leq 0 \tag{4.33}$$

for the internal friction $\tan\varphi$ of the material.

Accordingly, the following discontinuity angle is obtained from the stationarity condition (4.15)

$$\tan(2\theta^{\mathrm{cr}}) = \frac{\mathrm{sign}(t_m)}{\tan\varphi} \qquad \Longrightarrow \qquad \theta^{\mathrm{cr}} = \pm\Big(\frac{\pi}{4} - \frac{\varphi}{2}\Big) \tag{4.34}$$

Note that two values are obtained for θ^{cr}. Substitution of the normal and tangential tractions (t_n, t_m) given from Eq. (4.13) into the traction-based failure criterion (4.33) yields

$$F(\boldsymbol{\sigma}, q) = \frac{1}{2\cos\varphi}\Big[\big(\sigma_1 + \sigma_2\big)\sin\varphi + \big(\sigma_1 - \sigma_2\big)\Big] - q \le 0 \tag{4.35}$$

This is the stress-based Mohr-Coulomb criterion in the regime $\sigma_1 \ge \sigma_3 \ge \sigma_2$.

Remark 4.4 The Tresca criterion is recovered for the friction angle $\varphi = 0$. In the regime $\sigma_1 \ge \sigma_3 \ge \sigma_2$, it follows that $\theta^{\mathrm{cr}} = \pm\pi/4$. The corresponding traction- and stress-based failure criteria are expressed as

$$f(\boldsymbol{t}, q) = \big|t_m\big| - q \le 0, \qquad F(\boldsymbol{\sigma}, q) = \frac{\sigma_1 - \sigma_2}{2} - q \le 0 \tag{4.36}$$

which are the expected results. ☐

4.4.3. Von Mises (J_2) criterion

Let us consider the following traction-based failure criterion

$$f(\boldsymbol{t}, q) = \sqrt{3\Big(\frac{1}{4}t_n^2 + t_m^2\Big)} - q \le 0 \tag{4.37}$$

which is an ellipse on the $t_n - t_m$ plane as shown in Fig. 9(a).

Recalling the relations (4.13), it follows from the stationarity condition (4.15) that

$$\bigg[\frac{\sigma_1 + \sigma_2}{2} - \frac{3\big(\sigma_1 - \sigma_2\big)}{2}\cos(2\theta^{\mathrm{cr}})\bigg]\sin\big(2\theta^{\mathrm{cr}}\big) = 0 \tag{4.38}$$

Accordingly, if the conditions $2\sigma_1 - \sigma_2 \ge 0$ and $2\sigma_2 - \sigma_1 \le 0$ are satisfied, the discontinuity angle θ^{cr} is determined from

$$\cos\big(2\theta^{\mathrm{cr}}\big) = \frac{\sigma_1 + \sigma_2}{3\big(\sigma_1 - \sigma_2\big)} = \frac{s_1 + s_2}{s_1 - s_2} \tag{4.39}$$

With the above discontinuity angle θ^{cr}, substitution of the normal and tangential tractions (t_n, t_m) evaluated from Eq. (4.13) into Eq. (4.37) yields the classical von Mises criterion, i.e.,

$$F(\boldsymbol{\sigma}, q) = \sqrt{3J_2} - q \le 0 \tag{4.40}$$

for the second invariant $J_2 = \frac{1}{3}\big(\sigma_1^2 + \sigma_2^2 - \sigma_1\sigma_2\big)$ of the deviatoric stress tensor $\boldsymbol{s}$.

For the cases $2\sigma_1 - \sigma_2 < 0$ or $2\sigma_2 - \sigma_1 > 0$, the discontinuity angle θ^{cr} is determined from Eq. (4.38) as

$$\sin(2\theta^{\mathrm{cr}}) = 0 \quad \Longrightarrow \quad \begin{cases} \theta^{\mathrm{cr}} = 0 & 0 < \sigma_2 < \sigma_1 < 2\sigma_2 \\ \theta^{\mathrm{cr}} = \pi/2 & 2\sigma_1 < \sigma_2 < \sigma_1 < 0 \end{cases} \tag{4.41}$$

which yields the following stress-based failure criterion

$$F(\boldsymbol{\sigma}, q) = \begin{cases} \dfrac{\sqrt{3}}{2}\big|\sigma_1\big| - q \leq 0 & 0 < \sigma_2 < \sigma_1 < 2\sigma_2 \\ \dfrac{\sqrt{3}}{2}\big|\sigma_2\big| - q \leq 0 & 2\sigma_1 < \sigma_2 < \sigma_1 < 0 \end{cases} \tag{4.42}$$

The discontinuity angles θ^{cr} for different stress ratios σ_1/σ_2 are summarized in Table A.2, and the resulting stress-based failure criterion are depicted in Fig. 9(b). As shown in this figure, Eq. (4.42) introduces tension- and compression-extensions into the classical von Mises criterion (4.40). Note that this modification is indispensable not only for strain localization to occur in an inelastic solids characterized by the von Mises model (4.40) while guaranteeing the stress continuity condition (3.1), but also for the equivalence between traction- and stress-based approaches; see Wu and Cervera (2014b) for more discussion.

4.4.4. Drucker-Prager criterion

Finally, let us consider the following homogeneous traction-based failure criterion of degree $M = 2$

$$f(\boldsymbol{t}, q) = t_m^2 - \frac{4\alpha^2 - 1}{4\big(1 - \alpha^2\big)} t_n^2 + \frac{\alpha}{1 - \alpha} q t_n - \frac{1 + \alpha}{3\big(1 - \alpha\big)} q^2 \leq 0 \tag{4.43}$$

where the parameter $\alpha = (\rho - 1)/(\rho + 1) \in [0, 1)$ is determined in terms of the ratio $\rho := f_c/f_t \geq 1$ between the uniaxial compressive strength f_c and the tensile one f_t. Dependent on the value of the parameter α, the following three cases can be identified:

- $0 \leq \alpha < 1/2$ or $1 \leq \rho < 3$: The failure criterion (4.43) defines an ellipse on the $t_n - t_m$ plane. The von Mises criterion (4.37) is recovered for $\alpha = 0$.
- $\alpha = 1/2$ or $\rho = 3$: The failure criterion (4.43) becomes a parabola on the $t_n - t_m$ plane.
- $\alpha > 1/2$ or $\rho > 3$: The failure criterion (4.43) defines a hyperbola on the $t_n - t_m$ plane, with the left branch of interest expressed as

  $$\tan\varphi \cdot t_n + \sqrt{t_m^2 + \omega^2 q^2} - c \leq 0 \tag{4.44}$$

  where the parameters $\tan\varphi, \omega$ and c are expressed as

  $$\tan\varphi = \sqrt{\frac{4\alpha^2 - 1}{4\big(1 - \alpha^2\big)}}, \qquad \omega = \frac{1 + \alpha}{\sqrt{3\big(4\alpha^2 - 1\big)}}, \qquad c = \frac{\alpha\big(1 + \alpha\big)}{\sqrt{\big(4\alpha^2 - 1\big)\big(1 - \alpha^2\big)}} q \tag{4.45}$$

  Note that the variables $\tan\varphi$ and c represent the internal frictional angle and cohesion of the asymptotic Mohr-Coulomb criterion, respectively.

For the failure criterion (4.43), it follows from the stationarity condition (4.15) that

$$\cos(2\theta^{\text{cr}}) = \frac{-\big(4\alpha^2 - 1\big)\big(\sigma_1 + \sigma_2\big) + 4\alpha\big(1 + \alpha\big)q}{3\big(\sigma_1 - \sigma_2\big)} \tag{4.46}$$

Substituting the above result into Eqs. (4.13) and introducing the obtained normal and tangential tractions (t_n, t_m) into Eq. (4.43), one yields the following stress-based failure criterion

$$F(\boldsymbol{\sigma}, q) = J_2 - \frac{1}{3}\Big[\alpha I_1 - \big(1+\alpha\big)q\Big]^2 \leq 0 \tag{4.47}$$

with the left branch of interest expressed as

$$\frac{1}{1+\alpha}\Big(\alpha I_1 + \sqrt{3J_2}\Big) - q \leq 0 \tag{4.48}$$

where the first invariant I_1 and the second invariant J_2 in the case of plane stress are given by

$$I_1 = \sigma_1 + \sigma_2, \qquad J_2 = \frac{1}{3}\big(\sigma_1^2 + \sigma_2^2 - \sigma_1\sigma_2\big) \tag{4.49}$$

This is exactly the classical Drucker-Prager criterion.

When the discontinuity (band) is initiated, the failure criterion $F(\boldsymbol{\sigma}, q) = 0$ is activated, i.e.,

$$\sqrt{\frac{2}{3}}\,\big\|\boldsymbol{s}\big\| = \frac{2}{3}\,\Big[\big(1+\alpha\big)q - \alpha I_1\Big] \geq 0 \tag{4.50}$$

for the norm $\big\|\boldsymbol{s}\big\| := \sqrt{\boldsymbol{s}:\boldsymbol{s}} = \sqrt{2J_2}$ of the deviatoric stress tensor $\boldsymbol{s}$. Accordingly, the discontinuity angle (4.46) can be alternatively determined from

$$\cos(2\theta^{\text{cr}}) = \frac{2\sqrt{2/3}\,\alpha\big\|\boldsymbol{s}\big\| + s_1 + s_2}{s_1 - s_2} \tag{4.51}$$

if the conditions $\sigma_1 \geq \tilde{\alpha}_1\sigma_2$ and $\sigma_1 \geq \sigma_2/\tilde{\alpha}_2$ are satisfied, with $\tilde{\alpha}_1$ and $\tilde{\alpha}_2$ expressed as $\tilde{\alpha}_{1,2} := \frac{1}{2}\Big[1 \pm \alpha\,\sqrt{3/\big(1-\alpha^2\big)}\Big]$. The above discontinuity angle θ^{cr}, dependent on the stress ratio σ_1/σ_2 and model parameter α, is summarized in Table A.3 and depicted in Fig. 10.

Remark 4.5 For the parameter $\alpha \in [1/2, 1)$, the left branch of Drucker-Prager failure criterion (4.43) or (4.48) defines an open surface in the principal $\sigma_1 - \sigma_2$ space. Accordingly, there exists a limit value for the discontinuity angle θ^{cr}. Regarding the parabolic failure criterion (i.e., $\alpha = 1/2$) that opens to the left (i.e., $\sigma_1 < 0$), it follows that

$$\lim_{\sigma_2\to\sigma_1<0} \sin^2\theta^{\text{cr}} = \lim_{\sigma_2\to\sigma_1<0} -\frac{\big(2\sigma_2 - \sigma_1\big) + \sqrt{\sigma_1^2 + \sigma_2^2 - \sigma_1\sigma_2}}{3\big(\sigma_1 - \sigma_2\big)} = \frac{1}{2} \tag{4.52}$$

Namely, the limit discontinuity angle is $\lim_{\sigma_2\to\sigma_1<0}\theta^{\text{cr}} = 45°$. For the hyperbolic one with $\alpha \in (1/2, 1)$, the admissible stress ratio σ_1/σ_2 in the compression-compression quadrant (i.e., $\sigma_1 < 0$ and $\sigma_2 < 0$) is constrained by the value of parameter α, and so is the discontinuity angle θ^{cr}, i.e.,

$$\sin\theta^{\text{cr}} \leq \sqrt{\frac{\big(1+2\alpha^2\big)\sigma_1/\sigma_2 - 2\big(1-\alpha^2\big)}{3\big(\sigma_1/\sigma_2 - 1\big)}} \qquad \text{with} \qquad \frac{\sigma_1}{\sigma_2} \leq \frac{1 + 2\alpha^2 - \sqrt{3\big(4\alpha^2 - 1\big)}}{2\big(1-\alpha^2\big)} \tag{4.53}$$

For instance, it follows that $0° \leq \theta^{\text{cr}} \leq 33.74°$ for the parameter $\rho = 4.0$ or equivalently, $\alpha = 0.6$. □

5. Application to a generic failure criterion

In this section a generic traction-based failure criterion is considered in the conditions of plane stress. Depending on the involved material parameters, the failure surface defines either an ellipse, a parabola, a hyperbola or the product of two straight lines. The classical von Mises, Drucker-Prager and Mohr-Coulomb criteria are also recovered as particular examples.

5.1. Traction-based failure criterion

Without loss of generality, let us consider the following homogeneous traction-based failure criterion $f(\boldsymbol{t}, q) \leq 0$ of degree $M = 2$

$$f(\boldsymbol{t}, q) = t_m^2 - \frac{1}{2 - A_0}\left[\left(A_0 - \frac{1}{2}\right)t_n^2 - B_0 q t_n + \frac{1}{6}B_0^2 q^2\right] - C_0 q^2 \leq 0 \tag{5.1}$$

where the non-negative parameters B_0 and C_0 are related to the parameter $A_0 < 2$ through

$$B_0 = \frac{2 - A_0}{2}\big(\rho - 1\big) \geq 0, \qquad C_0 = \frac{2 - A_0}{6}\rho \geq 0 \tag{5.2}$$

with $\rho := f_c/f_t \geq 1$ being the ratio between the uniaxial compressive and tensile strengths f_c and f_t. Only for the parameters satisfying $A_0 \leq 1/2 + B_0^2/(6C_0)$ can the failure surface $f(\boldsymbol{t}, q) = 0$ intersect the axis t_n. It then follows from the relations (5.2) that the admissible parameter A_0 is within the range

$$A_0 \leq \frac{2(\rho^2 - \rho + 1)}{(\rho + 1)^2} \tag{5.3}$$

The residual strength $q(\kappa)$ is normalized so that its initial value is $q^0 = f_t$.

For the admissible parameter $A_0 \leq 2(\rho^2 - \rho + 1)/(\rho + 1)^2$, the following cases can be identified:

- $A_0 < \frac{1}{2}$: As shown in Figure 11(a), the failure criterion (5.1) defines an ellipse on the $t_n - t_m$ plane

  $$f(\boldsymbol{t}, q) = t_m^2 + \frac{\frac{1}{2} - A_0}{2 - A_0}\left(t_n + \frac{B_0}{1 - 2A_0}q\right)^2 - \left[\frac{B_0^2}{3\big(1 - 2A_0\big)} + C_0\right]q^2 \leq 0 \tag{5.4}$$

  with its foci on the axis t_n and centered at $t_n = -B_0 q/\big(1 - 2A_0\big)$. An interesting particular case corresponds to $\rho = 1.0$, i.e., $B_0 = 0$ and $C_0 = (2 - A_0)/6$. In this case, the failure criterion (5.4) becomes

  $$f(\boldsymbol{t}, q) = t_m^2 + \frac{\frac{1}{2} - A_0}{2 - A_0}t_n^2 - \frac{2 - A_0}{6}q^2 \leq 0 \tag{5.5a}$$

  or, equivalently,

  $$\sqrt{t_n^2 + \beta^{-2}\, t_m^2} - \frac{2 - A_0}{\sqrt{3\big(1 - 2A_0\big)}}q \leq 0 \tag{5.5b}$$

  for the parameter $\beta := \sqrt{(\frac{1}{2} - A_0)/(2 - A_0)} \in [0, 1]$. The failure criterion (5.5b) is exactly the one suggested by Camacho and Ortiz (1996); Pandolfi et al. (1999), Jirásek and Zimmermann (2001).

- $A_0 = \frac{1}{2}$: As shown in Figure 11(b), the failure criterion (5.1) is a parabola on the $t_n - t_m$ plane

  $$f(\boldsymbol{t}, q) = t_m^2 + \beta_1 q t_n - \beta_2 q^2 \leq 0 \tag{5.6}$$

  where the parameters β_1 and β_2 are expressed as

  $$\beta_1 = \frac{2}{3} B_0 = \frac{1}{2}(\rho - 1), \qquad \beta_2 = \frac{1}{9} B_0^2 + C_0 = \frac{1}{16}(\rho + 1)^2 \tag{5.7}$$

  The parabolic traction-based failure criterion has been adopted in the embedded discontinuity models (Ohlsson and Olofsson, 1997; Mosler, 2005).

- $\frac{1}{2} < A_0 < 2(\rho^2 - \rho + 1)/(\rho + 1)^2$, or equivalently, $B_0^2 > 3(2A_0 - 1)C_0$: As shown in Figure 11(c), the failure criterion (5.1) defines a hyperbola on the $t_n - t_m$ plane, with the left branch of interest expressed as

  $$\tan\varphi \cdot t_n + \sqrt{t_m^2 + \omega^2 q^2} - c \leq 0 \tag{5.8}$$

  where $\tan\varphi$ and c denote the friction coefficient and cohesion of the asymptotic Mohr-Coulomb criterion

  $$\tan\varphi = \sqrt{\frac{A_0 - 1/2}{2 - A_0}}, \qquad c = \frac{B_0 q}{\sqrt{2(2 - A_0)(2A_0 - 1)}} \tag{5.9a}$$

  together with the following parameter ω

  $$\omega = \sqrt{\frac{B_0^2}{3(2A_0 - 1)} - C_0} \tag{5.9b}$$

  Similar hyperbolic failure function has been adopted in the literature to describe the normal and shear coupling of cohesive cracks (Stankowski et al., 1993; Cervenka, 1994; Carol et al., 1997; Weihe et al., 1997; Most and Bucher, 2007).

- $A_0 = 2(\rho^2 - \rho + 1)/(\rho + 1)^2$, or equivalently, $B_0^2 = 3(2A_0 - 1)C_0$: As shown in Figure 11(d), the failure function (5.1) becomes the product of two straight lines on the $t_n - t_m$ plane. The left branch of interest correspond to $\omega = 0$ in the hyperbolic criterion (5.8), i.e.,

  $$\tan\varphi \cdot t_n + |t_m| - c \leq 0 \tag{5.10}$$

  where the internal friction coefficient $\tan\varphi$ and the cohesion c are given by

  $$\tan\varphi = \frac{1}{2} \frac{\rho - 1}{\sqrt{\rho}}, \qquad c = \frac{1}{2} \sqrt{\rho}\, q \tag{5.11}$$

  This is exactly the classical Mohr-Coulomb criterion considered in Section 4.4.2.

Remark 5.1 The traction-based failure criterion (4.43), which corresponds to the Drucker-Prager model discussed in Section 4.4.4, is recovered for the parameters (5.2) satisfying the relation $A_0 = B_0^2/(6C_0)$, or equivalently,

$$A_0 = 2\alpha^2, \qquad B_0 = 2\alpha(1 + \alpha), \qquad C_0 = \frac{1}{3}(1 + \alpha)^2 \tag{5.12}$$

where $\alpha := (\rho - 1)/(\rho + 1) \in [0, 1)$ is the material constant introduced before. The von Mises model considered in Section 4.4.3 then corresponds to $\alpha = 0$. □

5.2. Discontinuity angle and stress-based failure criterion

For the traction-based failure criterion (5.1), the discontinuity angle θ^{cr} is given from Eq. (4.15) by

$$\cos(2\theta^{\mathrm{cr}}) = \frac{2B_0 q + \big(1 - 2A_0\big)\big(\sigma_1 + \sigma_2\big)}{3\big(\sigma_1 - \sigma_2\big)} \tag{5.13}$$

With the above discontinuity, the corresponding stress-based failure criterion is obtained as

$$\begin{aligned} F(\boldsymbol{\sigma}, q) &= J_2 - \frac{1}{6} A_0 I_1^2 + \frac{1}{3} B_0 q I_1 - C_0 q^2 \\ &= \frac{2 - A_0}{6}\big(\sigma_1^2 + \sigma_2^2\big) - \frac{1 + A_0}{3}\sigma_1\sigma_2 + \frac{B_0}{3}(\sigma_1 + \sigma_2) q - C_0 q^2 \leq 0 \end{aligned} \tag{5.14}$$

which verifies the following function types

$$\begin{cases} A_0 < \frac{1}{2} & \text{Elliptical function; see Figure 12(a)} \\ A_0 = \frac{1}{2} & \text{Parabolic function; see Figure 12(b)} \\ \frac{1}{2} < A_0 < 2(\rho^2 - \rho + 1)/(\rho + 1)^2 & \text{Hyperbolic function; see Figure 12(c)} \\ A_0 = 2(\rho^2 - \rho + 1)/(\rho + 1)^2 & \text{Product of two straight lines; see Figure 12(d)} \end{cases} \tag{5.15}$$

As can be seen, the same function types are obtained as those of the traction-based failure criterion (5.1). Note that the functions similarly to Eq. (5.14) have been used in the modeling of dominant tensile failure in concrete-like quasi-brittle materials, both in the context of plasticity (Rosenthal and Glucklich, 1970; Ohtani and Chen, 1988; Kuhl et al., 2000) and damage mechanics (Comi and Perego, 2001).

When the discontinuity (band) is initiated, the failure criterion $F(\boldsymbol{\sigma}, q) = 0$ is activated so that

$$F(\boldsymbol{\sigma}, q) = 0 \qquad \Longrightarrow \qquad q = \alpha_r \sigma_1 \tag{5.16}$$

where the coefficient $\alpha_r \geq 1$ depends on the stress ratio $r := \sigma_2/\sigma_1$

$$\alpha_r = \frac{B_0\big(1 + r\big) \pm \sqrt{B_0^2\big(1 + r\big)^2 + 6A_r C_0}}{6C_0} \tag{5.17a}$$

$$A_r = \big(2 - A_0\big) - 2\big(1 + A_0\big) r + \big(2 - A_0\big) r^2 \tag{5.17b}$$

Accordingly, the discontinuity angle θ^{cr} given from Eq. (5.13) finally becomes

$$\cos(2\theta^{\mathrm{cr}}) = \frac{2B_0\alpha_r + \big(1 - 2A_0\big)\big(1 + r\big)}{3\big(1 - r\big)} \tag{5.18}$$

Clearly, it depends on the stress ratio $r := \sigma_2/\sigma_1$ which remains fixed for a proportional load path.

Remark 5.2 For the model parameters satisfying $B_0^2 = 3(2A_0 - 1)C_0$, i.e., $A_0 = 2(\rho^2 - \rho + 1)/(\rho + 1)^2$, the failure criterion (5.14) becomes

$$F(\boldsymbol{\sigma}, q) = \frac{\rho\sigma_1 - \sigma_2 - \rho q}{\rho + 1} \cdot \frac{\sigma_1 - \rho\sigma_2 + \rho q}{\rho + 1} \leq 0 \tag{5.19}$$

The left branch of interest coincides with the classical Mohr-Coulomb criterion (4.35), i.e.,

$$\frac{\rho\sigma_1 - \sigma_2 - \rho q}{\rho + 1} = \frac{1}{2}\Big[\big(\sigma_1 + \sigma_2\big)\sin\varphi + \big(\sigma_1 - \sigma_2\big) - q\big(1 + \sin\varphi\big)\Big] \leq 0 \tag{5.20}$$

for the following internal friction angle $\varphi \in [0, \pi/2]$

$$\sin\varphi = \frac{\rho - 1}{\rho + 1} \qquad \Longleftrightarrow \qquad \rho = \frac{1 + \sin\varphi}{1 - \sin\varphi} \tag{5.21}$$

Note that the Mohr-Coulomb criterion (5.20) applies for $\sigma_1 \geq 0$ and $\sigma_2 \leq 0$ in the plane stress condition ($\sigma_3 = 0$). □

5.3. Parameter calibration

In the literature (Stankowski et al., 1993; Cervenka, 1994; Carol et al., 1997; Weihe et al., 1997; Most and Bucher, 2007), different forms of hyperbolic traction-based failure criteria have been proposed for the modeling of localized failure in quasi-brittle materials, owing to the excellent data fitting capabilities and other advantageous features (e.g., no slope discontinuity at the tip, asymptotically approaching to Mohr-Coulomb criterion for increasing compression, and a constant friction angle, etc.). For instance, the following traction-based failure criterion (Carol et al., 1997; Most and Bucher, 2007) can be considered

$$\tan\varphi \cdot t_n + \sqrt{t_m^2 + \big(c - \chi \cdot \tan\varphi\big)^2} - c \leq 0 \tag{5.22}$$

where χ denotes the failure strength, not necessarily identical to the macroscopic material tensile strength f_t; $\tan\varphi$ and c represent the friction and cohesion of the asymptotic Mohr-Coulomb criterion. However, the involved parameters are essentially mesoscopical entities hard to be determined from standard experimental tests. This shortcoming restrains heavily their application. Here, a rational approach is suggested.

For the model parameter $\frac{1}{2} < A_0 < 2(\rho^2 - \rho + 1)/(\rho + 1)^2$, the traction-based failure criterion (5.22) coincides with the one (5.8), with

$$\omega q = c - \chi \cdot \tan\varphi \qquad \Longleftrightarrow \qquad \chi = \frac{c - \omega q}{\tan\varphi} \tag{5.23}$$

That is, all the involved parameters can be determined, provided the parameter A_0 and the material constant $\rho = f_c/f_t$ are known by fitting the stress-based failure criterion (5.14) with available macroscopic test data.

Let us consider a strength ratio $\rho := f_c/f_t = 10$, typical for concrete. In order for a discontinuity (band) characterized by the traction-based failure criterion (5.8) or (5.22) to form in the softening solid described by the stress-based counterpart (5.14), the model parameter A_0 has to be in the range $A_0 \in (0.5, 1.504)$. As shown in Figure 13(a), the biaxial strength envelope corresponding to the following parameters

$$A_0 = 1.45 \qquad \Longrightarrow \qquad B_0 = 2.475, \qquad C_0 = 0.917 \tag{5.24}$$

fits the test data of normal concrete in tension-tension and tension-compression rather well. It follows from the relations (5.9) and (5.23) that

$$\tan\varphi = 1.314, \qquad c = 1.712q, \qquad \chi = q \tag{5.25}$$

The corresponding traction-based failure criterion is shown in Figure 13(b).

5.4. *Example: Willam's numerical test*

To validate the above closed-form results and calibrated parameters associated with the hyperbolic failure criterion (5.8) or (5.22), Willam's numerical test is considered (Willam et al., 1987). This test is an artificially constructed benchmark characterized by rotations of the principal strain/stress axes. It has been widely used to assess the performance of constitutive models for concrete (Rots, 1988; Weihe et al., 1997; Carol et al., 2001; Wu and Xu, 2011). The loading scenario of Willam's numerical test is strain-controlled, consisting of two stages: (*i*) the material is stretched uniaxially along axis x, leading to strains with the incremental ratio $\Delta\epsilon_{xx} : \Delta\epsilon_{yy} : \Delta\epsilon_{xy} = 1 : -\nu_0 : 0$, until the stress σ_{xx} reaches its maximum value (i.e., the tensile strength) f_t, with ν_0 being the material Poisson's ratio; (*ii*) a combination of strains with the incremental ratio $\Delta\epsilon_{xx} : \Delta\epsilon_{yy} : \Delta\epsilon_{xy} = 1 : 1.5 : 1$ is then applied until the complete failure of the material. In general, a constitutive model is said to pass Willam's numerical test if the following two conditions are satisfied (Rots, 1988): (a) the predicted maximum principal stress σ_1 does not exceed the tensile strength f_t and (b) all computed stress components tend to zero asymptotically.

The traction-based elastoplastic damage model discussed in Section 3.3 is extended to consider multiple cracks; see Wu and Xu (2011) for the details. Furthermore, the following hyperbolic softening law is adopted

$$q(\kappa) = f_t\Big[1 - \big(1 + \kappa/\kappa_u\big)^{-\eta}\Big] \tag{5.26}$$

for the uniaxial tensile strength f_t. The parameter κ_u is related to the specific fracture energy g_{f} through the crack band theory (2.29), i.e.,

$$g_{\mathrm{f}} = \frac{G_{\mathrm{f}}}{b} = \Big(1 - \frac{1}{2}\xi\Big)\int_0^\infty q(\kappa)\,\mathrm{d}\kappa \qquad \Longrightarrow \qquad \kappa_u = \frac{(\eta - 1)g_{\mathrm{f}}}{\big(1 - \frac{1}{2}\xi\big)f_t} \tag{5.27}$$

where the parameter $\eta > 1$ controls the initial slope and shape of the softening curve, as shown in Fig. 14. As the parameter η increases, the hyperbolic softening function (5.26) converges to the exponential one frequently adopted in the literature (Wu and Xu, 2011).

In the numerical simulation, the material properties are assumed as follows: Young's modulus $E_0 = 3.0\times10^4$MPa, Poisson's ratio $\nu_0 = 0.2$, tensile strength $f_t = 3$MPa. Furthermore, a plastic/damage parameter $\xi = 0.5$ is taken, together with the hyperbolic softening function (5.26) with a specific mode-I fracture energy $g_{\mathrm{f}} = 450\text{N/m}^2$ and a softening parameter $\eta = 10$. The above data correspond to those given in Weihe et al. (1997), except that a plasticity model was adopted therein. Plane stress state is assumed. Accordingly, the stress-based failure criterion (5.14) with $q^0 = f_t$ is used to determine the instant of initiating a discontinuity (band), with its orientation given by the analytical solution (5.18).

The predicted evolution curves of the principal stresses σ_1 and σ_2 with the prescribed normal strain ϵ_{xx} are shown in Figure 15(a). For comparison, the result under uniaxial tension is also plotted. The evolution curves of stress components σ_{xx}, σ_{yy} and σ_{xy} given in Figure 15(b) demonstrate that the aforementioned criterion are satisfied and the Willam's numerical test is passed.

The above results deserve further discussion. In accordance with the solution (5.18) for the failure criterion (5.14), a primary crack normal to the stress σ_{xx} is initiated at the end of the first step, with no shear stress σ_{xy}. In the second step, the normal strain ϵ_{xx} continues increasing, leading to softening accompanied with certain amounts of shear strains/stresses. Meanwhile, the strains and stresses growing in other directions cause the current major principal stress progressively to be inclined to the primary crack. The rotation of the principal stress axes initiates a secondary crack in an inclination of 74.07° with respect to the primary one. The additional softening mechanism caused by the secondary crack deactivates the primary one. The interaction of the decreasing stress σ_{xx} and the other increasing ones (i.e. σ_{yy} and σ_{xy}) leads to an initially decreasing principal stress σ_1 which sooner or later increases to a second stress apex. In contrast, due to the initial softening and subsequent unloading mechanism the stress component σ_{xx} nearly always decreases, accompanied with an oscillation regime signifying the primary crack is reactive. Subsequently, both cracks remain active during the rest loading history, with all stress components progressively vanishing. The above results are qualitatively similar, but not identical, to those obtained in the literature (Weihe et al., 1997; Carol et al., 2001; Wu and Xu, 2011), though all of them pass the Willam's numerical test.

6. Conclusions

In this work, localized failure in solids is approached by embedding or smearing a traction-based inelastic discontinuity (band) within an (equivalent) elastic matrix (with or without stiffness damage or plastic strains prior to strain localization). The conformity of the strong/regularized and embedded/smeared discontinuity approaches are systematically investigated, regarding the strategies dealing with the kinematics (displacement and strain fields) and statics (stress field and traction continuity).

In the strong and regularized discontinuity approaches, the traction continuity condition is imposed in weak form. Accordingly, the (apparent) displacement jumps are retained as independent variables, so that constitutive laws for both the bulk and the discontinuity (band) have to be provided in oder to solve the corresponding boundary value problems. Based on the irreversible thermodynamics with internal variables, consistent cohesive model in terms of tractions vs. jumps and the regularized version in terms of tractions vs. inelastic deformations are established for the discontinuity (band), in addition to the elastic bulk. Particularly, associated damage and plastic evolution laws are derived from the postulate of maximum energy dissipation constrained by a given traction-based failure criterion. The inter-relations between the kinematics, constitutive laws and fracture energy demonstrate that the strong discontinuity approach and the regularized one are consistently related. That is, the strong discontinuity is the limit of a regularized one with a vanishing band width; reciprocally, the regularized discontinuity can be regarded as the convenient regularization of a strong one.

Alternatively, the traction continuity condition can also be enforced point-wisely in strong form, so that the standard principle of virtual work applies. Though the strain field may be discontinuous or even singular upon strain localization, as the inelastic strains are localized completely within the discontinuity (band), the elastic strain field and the resulting stress field are both continuous in the entire solid. In this case, the traction continuity condition recovers the classical static constraint through which the kinematic variables associated with the (apparent) displacement jumps can be eliminated at the material level. This strategy leads to the embedded/smeared discontinuity models for overall inelastic behavior of solids. Furthermore, they can also be cast into the elastoplastic degradation framework with a different kinematic decomposition. The above facts motivates the alternative methodology for modeling localized failure, i.e., strain localization of a stress-based inelastic softening solid.

As an indispensable ingredient of the above traction-based approaches, the discontinuity orientation is determined from Mohr's maximization postulate. This choice is justified by the fact that, in the case of associated evolution laws, the discontinuity orientation determined from strain localization analysis coincides with that obtained from Mohr's maximization postulate. Closed-form results are presented in plane stress conditions, with the classical Rankine, Mohr-Coulomb, von Mises and Drucker-Prager criteria as illustrative examples.

Finally, a generic failure criterion of either elliptic, parabolic or hyperbolic type, appropriate for the modeling of mixed-mode failure, is analyzed in a unified manner. The corresponding stress-based failure criterion is determined, so that the involved mesoscopic parameters can be calibrated from available macroscopic test data. In this way, the deficiency hindering its practical application is largely removed as shown in the Willam's numerical test.

7. Acknowledgements

Support from the Spanish Ministry of Economy and Competitivity under the project Enhanced Accuracy Computational Framework for Strain Localization and Failure Mechanisms (EACY) – is acknowledged by the first author (M. Cervera). The second author (J.Y. Wu) acknowledges support from the National Natural Science Foundation of China (51222811, 51008130) and the State Key Laboratory of Subtropic Building Science (2015ZB24).

Appendix A. Proof of equivalence between Eqs. (3.9) and (3.25a)

The *Sherman-Morrison-Woodbury formula* states that a rank k correction to a matrix results in a rank k correction of the inverse (Golub and van Loan, 1996), i.e.,

$$\left(\boldsymbol{A}+\boldsymbol{a}\boldsymbol{b}^{\mathrm{T}}\right)^{-1}=\boldsymbol{A}^{-1}-\boldsymbol{A}^{-1}\boldsymbol{a}\left(\boldsymbol{1}+\boldsymbol{b}^{\mathrm{T}}\boldsymbol{A}^{-1}\boldsymbol{a}\right)^{-1}\boldsymbol{b}^{\mathrm{T}}\boldsymbol{A}^{-1} \tag{A.1}$$

where $\boldsymbol{A}$ is a rank $k \times k$ matrix; $\boldsymbol{a}$ and $\boldsymbol{b}$ are both $k \times j$ matrices; $\boldsymbol{1}$ is a rank $j \times j$ identity matrix.

To prove the equivalence, on the one hand, let us write the tangent compliance (3.12) as the following matrix form

$$\mathbb{C}_{\tan}=\mathbb{C}^0+\boldsymbol{\mathcal{N}}\boldsymbol{C}^{\mathrm{d}}_{\tan}\boldsymbol{\mathcal{N}}^{\mathrm{T}} \tag{A.2}$$

where $\boldsymbol{\mathcal{N}}$ is the Voigt matrix representation of the third-order tensor $\mathcal{N}_{ijk}=\frac{1}{2}\left(n_i\delta_{jk}+n_j\delta_{ik}\right)$ introduced in Eq. (3.20b). It follows from the Sherman-Morrison-Woodbury formula (A.1) that

$$\mathbb{E}_{\tan}=\mathbb{E}^0-\mathbb{E}^0\boldsymbol{\mathcal{N}}\left(\boldsymbol{E}^{\mathrm{d}}_{\tan}+\boldsymbol{\mathcal{N}}^{\mathrm{T}}\mathbb{E}^0\boldsymbol{\mathcal{N}}\right)^{-1}\boldsymbol{\mathcal{N}}^{\mathrm{T}}\mathbb{E}^0 \tag{A.3}$$

which is exactly the matrix form of the tangent stiffness (3.9).

On the other hand, the tangent compliance (3.25b) can also be expressed as the following matrix form

$$\mathbb{C}_{\tan} = \mathbb{C} + \frac{\boldsymbol{\varLambda}\boldsymbol{\varLambda}^{\mathrm{T}}}{h \cdot H \cdot h} \tag{A.4}$$

Accordingly, it follows from the Sherman-Morrison-Woodbury formula (A.1) that

$$\mathbb{E}_{\tan} = \mathbb{C}_{\tan}^{-1} = \mathbb{E} - \frac{\mathbb{E}\boldsymbol{\varLambda}\boldsymbol{\varLambda}^{\mathrm{T}}\mathbb{E}}{\boldsymbol{\varLambda}^{\mathrm{T}}\mathbb{E}\boldsymbol{\varLambda} + h \cdot H \cdot h} \tag{A.5}$$

which is exactly the matrix expression of the tangent stiffness (3.25a).

Calling for the relation (2.26b) and the dissipative flow tensor $\boldsymbol{\varLambda}$ in Eq. (3.20), the equivalence between the tangent compliance tensors (3.12) and (3.25b) can be established, i.e.,

$$\mathbb{C}_{\tan} = \mathbb{C}^0 + \big(\boldsymbol{C}^{\mathrm{d}}_{\tan} \overline{\underline{\otimes}} \boldsymbol{N}\big)^{\mathrm{sym}} = \mathbb{C}^0 + \big(\boldsymbol{C}^{\mathrm{d}} \overline{\underline{\otimes}} \boldsymbol{N}\big)^{\mathrm{sym}} + \frac{\boldsymbol{\varLambda} \otimes \boldsymbol{\varLambda}}{h \cdot H \cdot h} = \mathbb{C} + \frac{\boldsymbol{\varLambda} \otimes \boldsymbol{\varLambda}}{h \cdot H \cdot h} \tag{A.6}$$

Therefore, the tangent stiffness tensors (3.9) and (3.25a) are also equivalent.

References

Armero, F., 1999. Large-scale modeling of localized dissipative mechanisms in a local continuum: applications to the numerical simulation of strain localization in rate-dependent inelastic solids. *Mech. Cohes.-Frict. Mater.*, 4: 101-131.

Armero, F. and Oller, S., 2000. A general framework for continuum damage models. I: Infinitesimal plastic damage models in stress space. *Int. J. Solids Structures*, 37: 7409-7464.

Barenblatt, G.I., 1959. The formation of equilibrium cracks during brittle fracture. General ideas and hypotheses. Axially-symmetric cracks. *J. Applied Mathematics and Mechanics*, 23: 622-636.

Barenblatt, G.I., 1962. The mathematical theory of equilibrium cracks in brittle fracture. *Adv. Appl. Mech.*, 7: 55-129.

Bažant, Z.P. and Oh, B.H. Crack band theory for fracture of concrete. Materials and Structures (RILEM, Paris), 1983, 16: 155–177.

Camacho G.T. and Ortiz M., 1996. Computational modeling of impact damage in brittle materials. *Int. J. Solids Structures*, 33: 2899-2938.

Carol, I., Prat, P., and López, C., 1997. Normal/shear cracking model: application to discrete crack analysis. *J. Eng. Mech., ASCE*, 123(8): 765-773.

Carol, I., Rizzi, E., Willam, K., 1994. A unified theory of elastic degradation and damage based on a loading surface. *Int. J. Solids Structures*, 31(20): 2835-2865.

Carol, I., Rizzi, E. and Willam, K., 2001. On the formulation of anisotropic elastic degradation. I: Theory based on a pseudo-logarithmic damage tensor rate; II: Generalized pseudo-Rankine model for tensile damage. *Int. J. Solids Structures*, 38(4): 491-546.

Cervera, M., 2008a. A smeared-embedded mesh-corrected damage model for tensile cracking. *Int. J. Numer. Meth. Engng.*, 76: 1930-1954.

Cervera, M., 2008b. An othortropic mesh corrected model. *Comput. Methods Appl. Mech. Engrg.*, 197: 1603-1619.

Cervera, M., Chiumenti, M. and Di Capua, D., 2012. Benchmarking on bifurcation and localization in J_2 plasticity for plane stress and plane strain conditions. *Comput. Methods Appl. Mech. Engrg.*, 241-244: 206-224.

Cervenka, J., 1994. Discrete Crack Modelling in Concrete Structures. Ph.D. Thesis, University of Colorado, Boulder.

Chen, W.F., 1994. Constitutive equations for engineering materials: plasticity and modeling, vol. 2. Elsevier, Amsterdam.

Coleman, B.D. and Gurtin, M.E., 1967. Thermodynamics with internal state variables. *J. Chem. Phys.* 47: 597-613.

Comi, C. and Perego, U., 2001. Fracture energy based bi-dissipative damage model for concrete. *Int. J. Solids Structures*, 38: 6427-6454.

Dougill, J.W., 1976. On stable progressively fracturing solids. *J. Appl. Mech. Phys.*, 27: 423-437.

Dugdale, D., 1960. Yielding of steel sheets containing slits. *J. Mech. Phys. Solids*, 8: 100-108.

Golub, G.H. and van Loan, C.F., 1996. Matrix computations, third edition (page 50). The John Hopkins University Press, Baltimore.

Hill, R., 1958. General theory of uniqueness and stability of elasto-plastic solids. *J. Mech. Phys. Solids*, 6: 236–249.

Hill, R., 1962. Acceleration waves in solids. *J. Mech. Phys. Solids*, 10: 1–16.

Hillerborg, A., Modeer, M. and Petersson, P.E., 1976. Analysis of crack formation and crack growth in concrete by means of fracture mechanics and finite elements. *Cement Concrete Res.*, 6: 773-782.

Hueckel, T. and Maier, G., 1977. Incrementarlly boundary value problems in the presense of coupling of elastic and plastic deformations: a rock mechanics oriented theory. *Int. J. Solids Structures*, 13: 1-15.

Itskov, M., 2007. *Tensor algebra and tensor analysis for engineers: with applications to continuum mechanics*. Springer, Berlin.

Jirásek, M., 2000. Comparative study on finite elements with embedded discontinuities. *Comput. Methods Appl. Mech. Engrg.*, 188: 307–330.

Jirásek, M. and Zimmermann, T., 2001. Embedded crack model. *Internat. J. Numer. Methods Engrg.*, 50(6): 1269-1290.

Krajcinovic, D., 2003. Damage mechanics. Elsevier B.V., Netherlands.

Kuhl, E., Ramm, E. and Willam, K., 2000. Failure analysis of elasto-plastic material models on different levels of observation. *Int. J. Numer. Meth. Engng*, 46: 1673-1698.

Malvern, L.E., 1969. Introduction to the mechanics of a continuous medium. Prentice-Hall International, Englewood Cliffs, New Jersey.

Meschke, G, Lackner, R. and Mang, H.A., 1998. An anisotropic elastoplastic damage model for plain concrete. *Int. J. Numer. Meth. Engng.*, 42: 703-727.

Moës, N., Dolbow, J. and Belytschko, T., 1999. A finite element method for crack growth without remeshing. *Int. J. Numer. Meth. Engng*, 46: 131-150.

Mohr, O., 1900. Welche Umstände bedingen die Elastizitätsgrenze und den Bruch eines Materials? *Civilingenieur: Zeitschrift des Vereins deutscher Ingenieure*, VDI 44/45: 1524-1530; 1572-1577.

Mosler, J., 2005. On advanced solution strategies to overcome locking effects in strong discontinuity approaches. *Int. J. Numer.*

Meth. Engng., 63: 1313-1341.

Most, T. and Bucher, C., 2007. Energy-based simulation of concrete cracking using an improved mixed-mode cohesive crack model within a meshless discretization. *Int. J. Numer. Anal. Meth. Geomech.*, 31: 285-305.

Ngo, D. and Scordelis, A.C., 1967. Finite element analysis of reinforced concrete beams, *ACI J.*, 64(14): 152-163.

Ohlsson, U. and Olofsson, T., 1997. Mixed-mode fracture and anchor bolts in concrete analysis with inner softening bands. *Journal of Engineering Mechanics*, ASCE, 123: 1027-1033.

Oliver, J., 1996. Modeling strong discontinuities in solid mechanics via strain softening contitutive equations. Part I: Fundaments & Part II: Numerical simulation. *Int. J. Numer. Meth. Engng*, 39: 3575-3623.

Oliver, J., Cervera, M. and Manzoli, O. 1998. On the use of strain-softening models for the simulation of strong discontinuities in solids. *Material instabilities in solids*: 107-123, Wiley.

Oliver, J. Cervera, M. and Manzoli, O., 1999. Strong discontinuities and continuum plasticity models: the strong discontinuity approach. *International Journal of Plasticity*, 15: 319-351.

Oliver, J., 2000. On the discrete constitutive models induced by strong discontinuity kinematics and continuum constitutive equations. *Int. J. Solids Structures*, 37: 7207-7229.

Ohtani, Y. and Chen, W.F., 1988. Multple hardening plasticity for concrete material. *Journal of Engineering Mechanics, ASCE*, 114: 1890–1910.

Ortiz., M., 1985. A constitutive theory for the inelastic behavior of concrete. *Mech. Mater.*, 4: 76-93.

Ottosen, N. and Runesson, K., 1991a. Properties of bifurcation solutions in elasto-plasticity. *Int. J. Solids Structures*, 27: 401-421.

Ottosen, N. and Runesson, K., 1991b. Discontinuous bifurcations in a non-associated Mohr material. *Mech. Mater.*, 12: 255-265.

Pandolfi, A., Krysl, P. and Ortiz, M., 1999. Finite element simulation of ring expansion and fragmentation: the capturing of length and time scales through cohesive models of fracture. *Int. J. Fracture*, 95: 279-297.

Rashid, Y., 1968. Analysis of prestressed concrete pressure vessels. *Nuclear Engineering and Design*, 7: 334-344.

Rice, J.R. and Rudnicki, J.W., 1980. A note on some features of the theory of localization of deformation. *Int. J. Solids Structures*, 16: 597-605.

Rosenthal, I. and Glucklich, J., 1970. Strength of plain concrete under biaxial stress. ACI Journal, 67: 903–914.

Rots, J.G., et al., 1985. Smeared crack approach and fracture localization in concrete. *Heron*, 30: 1-47.

Rots, J.G., 1988. Computational modeling of concrete fracture. *Doctoral Dissertation*, Delft University of Technology, Delft, The Netherlands.

Rots, J.G. and Blaauwendraad, J., 1989. Crack models for concrete: discrete or smeared? fixed, multi-directional or rotating? *Heron*, 34(1): 1-59.

Rudnicki, J.W. and Rice, J.R., 1975. Conditions of the localization of deformation in pressure-sensitive dilatant material. *J. Mech. Phys. Solids*, 23: 371–394.

Runesson, K., Ottosen, N.S. and Peric, D., 1991. Discontinuous bifurcations of elastic-plastic solutions at plane stress and plane strain. *Int. J. of Plasticity*, 7: 99-121.

Simó, J.C. and Ju, J.W., 1987. Strain- and stress-based continuum damage models. I: Formulation; II: Computational aspects. *Int. J. Solids Structure*, 23(7): 821-869.

Simó, J.C., Oliver, J. and Armero, F., 1993. An analysis of strong discontinuities induced by strain-softening in rate-independent inelastic solids. *Computational Mechanics*, 12: 277-296.

Stankowski, T., Runesson, K. and Sture, S., 1993. Fracture and slip of interfaces in cementitious composites. I: Characteristics, II: Implementation. *J. Engrg. Mech.*, 90: 845-867.

Steinmann, P. and Willam, K., 1991. Localization within the framework of micropolar elastoplasticity. *Advances in Continuum Mechanics*, VI: 296-313.

Thomas, T.Y., 1961. *Plastic Flow and Fracture of Solids*. Academic Press, New York.

Weihe, S., Kröplin, B. and de Borst R., 1997. Classification of smeared crack models based on material and structural properties. *Int. J. Solids Structures*, 35(5): 467-484.

Wells, G.N. and Sluys, L.J., 2001b. A new method for modelling cohesive cracks using finite elements. *Int. J. Numer. Meth. Engng.*, 50: 2667-2682.

Willam, K.J., Pramono, E. and Sture, S., 1987. Fundamental issues of smeared crack models. In: S.P. Shah and S.E. Swartz (Eds), *SEM/RILEM, International Conference on Fracture of Concrete and Rock*: 142-153.

Wu, J. Y., 2011. Unified analysis of enriched finite elements for modeling cohesive cracks. *Comput. Methods Appl. Mech. Engrg.*, 200(45-46): 3031-3050.

Wu, J. Y. and Cervera, M., 2013. Strain localization in elastoplastic damage solids. In: *Proceedings of International Symposium on Innovation & Sustainability of Structures in Civil Engineering (ISISS-2013)*, Harbin, China.

Wu, J. Y. and Cervera, M., 2014a. On the stress continuity condition for strain localization in softening solids. In: *Proceedings of 11th World Congress On Computational Mechanics (WCCM-2014)*, Barcelona, Spain.

Wu, J. Y. and Cervera, M., 2014b. Strain localization and failure mechanics for elastoplastic damage solids. *Monograph CIMNE*, M147, Barcelona, Spain.

Wu, J.Y. and Xu, S.L., 2011. An augmented multicrack elastoplastic damage model for tensile cracking. *Int. J. Solids Structures*, 48:2511-2528.

Wu, J.Y. and Xu, S.L., 2013. Reconsideration on the elastic damage/degradation theory for the modeling of microcrack closure-reopening (MCR) effects. *Int. J. Solids Structures*, 50(5): 795-805.

Wu, J. Y., Li, F. B. and Xu, S. L., 2015. Extended embedded finite elements with continuous displacement jumps for the modeling of localized failure in solids. *Comput. Methods Appl. Mech. Engrg.*, 285: 346-378.

Table A.2: Discontinuity angles θ^{cr} for the von Mises criterion in the plane stress conditions

	Stress ratio σ_1/σ_2							
	-1: -2	-1: -5	0: -1	1: -5	1: -1	1: 0	1: 0.25	1: 0.5
θ^{cr}	90.00°	60.00°	54.74°	51.42°	45.00°	35.26°	28.12°	0.00°

Table A.3: Discontinuity angles θ^{cr} for the Drucker-Prager criterion in plane stress conditions

f_c/f_t	Stress ratio σ_1/σ_2										
	-1: -1.24	-1: -2	-1: -5	0: -1	1: -5	1: -1	1: -0.5	1: -0.25	1: -0.15	1: 0	1 : 0.19
2.00	90.00°	51.65°	44.74°	41.81°	39.52°	33.68°	29.90°	26.30°	24.15°	19.47°	0.00°
3.00	43.48°	40.55°	37.35°	35.26°	33.32°	27.37°	22.82°	17.90°	14.51°	0.00°	0.00°
4.00	—	33.66°	32.69°	31.09°	29.33°	23.07°	17.62°	10.53°	0.00°	0.00°	0.00°

List of Figures

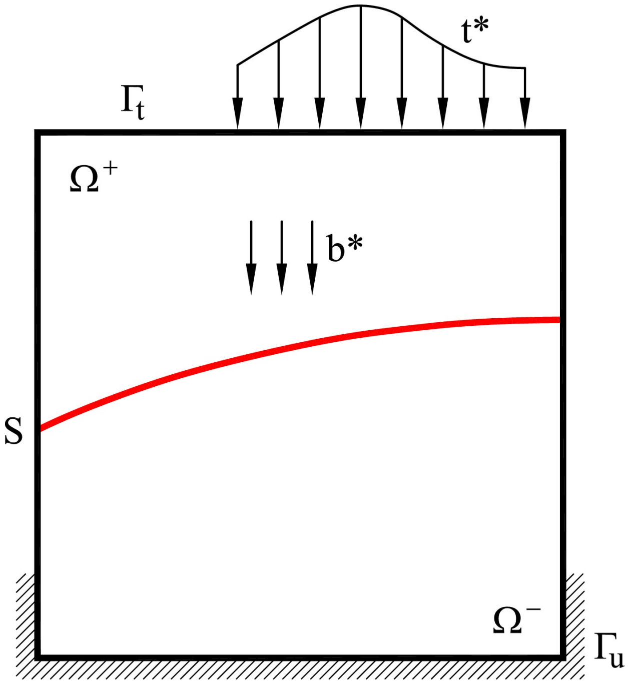

Figure 1: Problem setting in a solid medium with an internal discontinuity

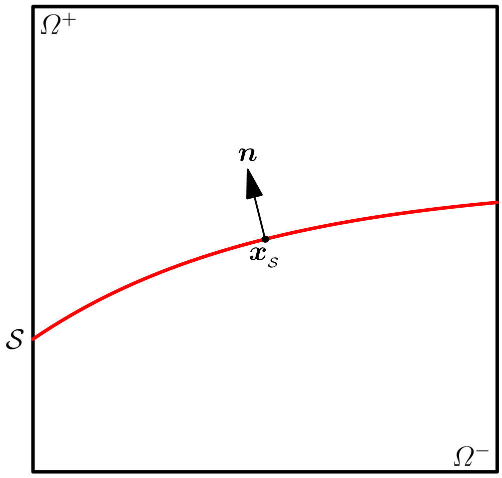

(a) Strong discontinuity in a solid

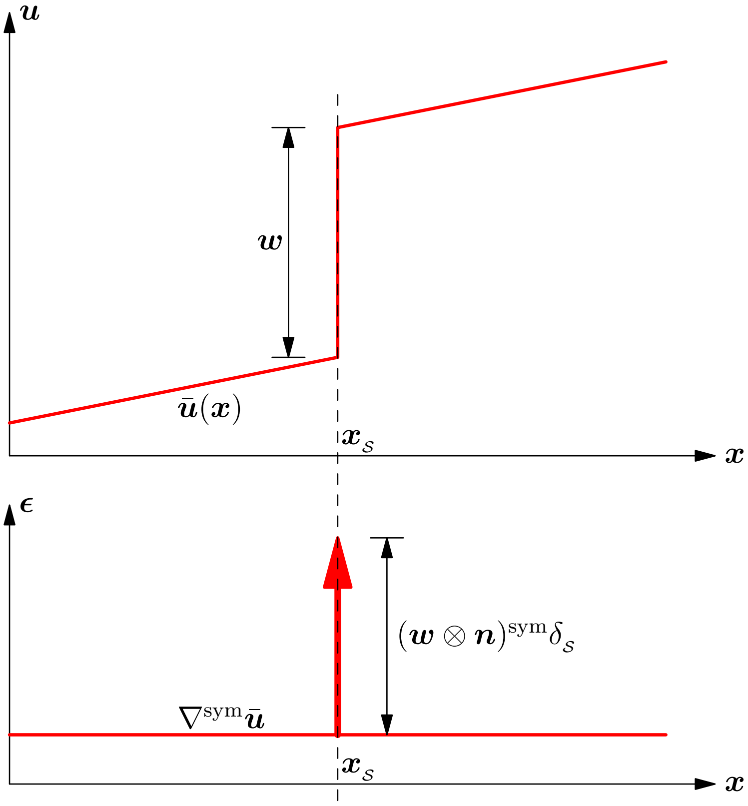

(b) Displacement and strain fields

Figure 2: Kinematics of a strong discontinuity

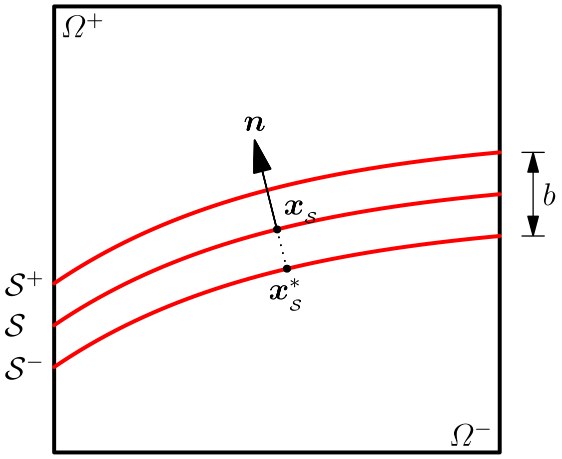

(a) Regularized discontinuity in a solid

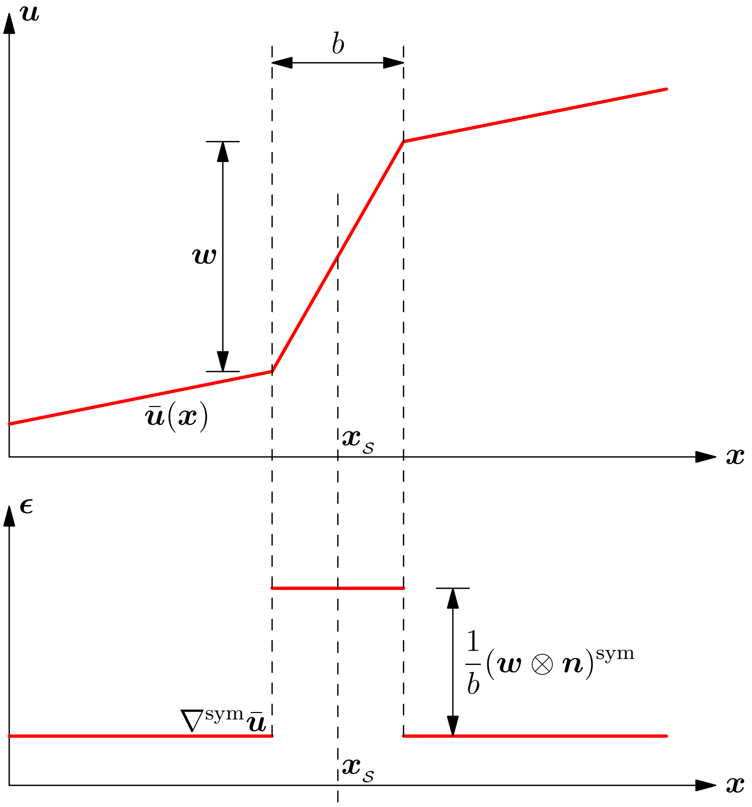

(b) Displacement and strain fields

Figure 3: Kinematics of a regularized discontinuity

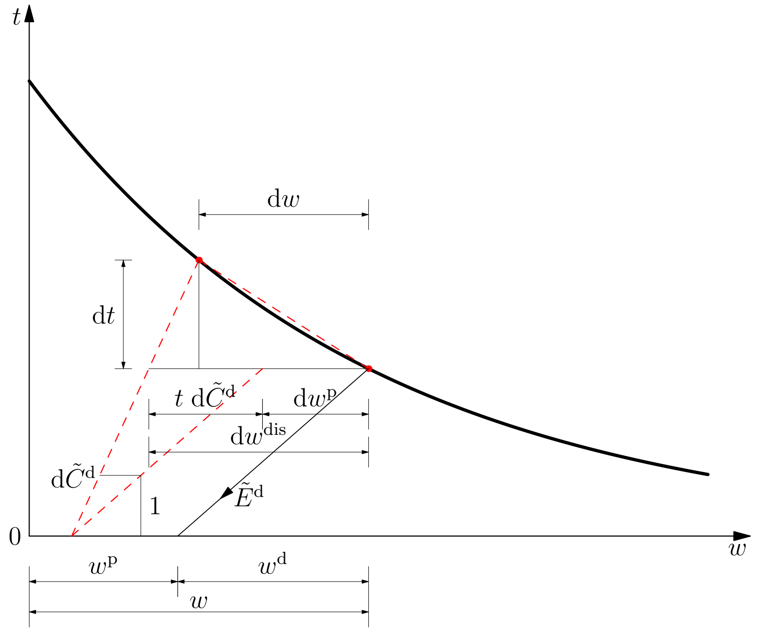

Figure 4: 1-D cohesive model for a strong discontinuity

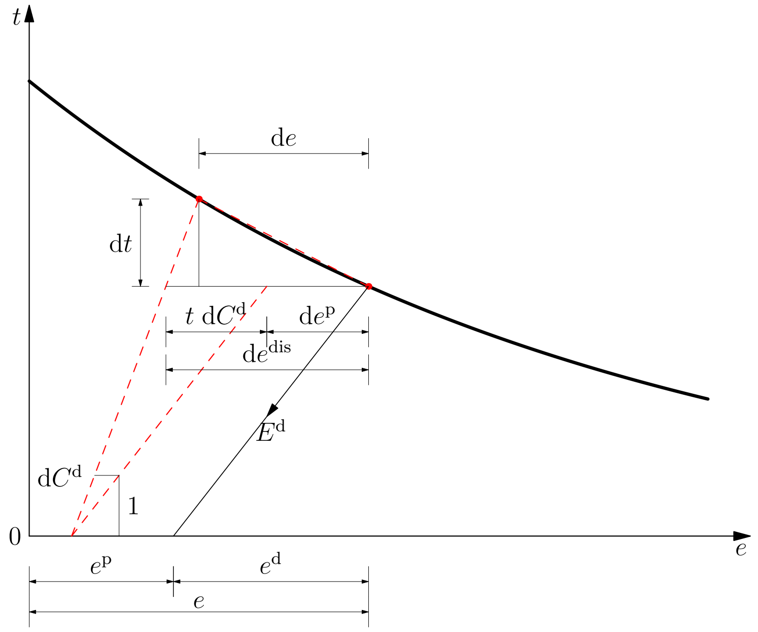

Figure 5: 1-D cohesive model for a regularized discontinuity

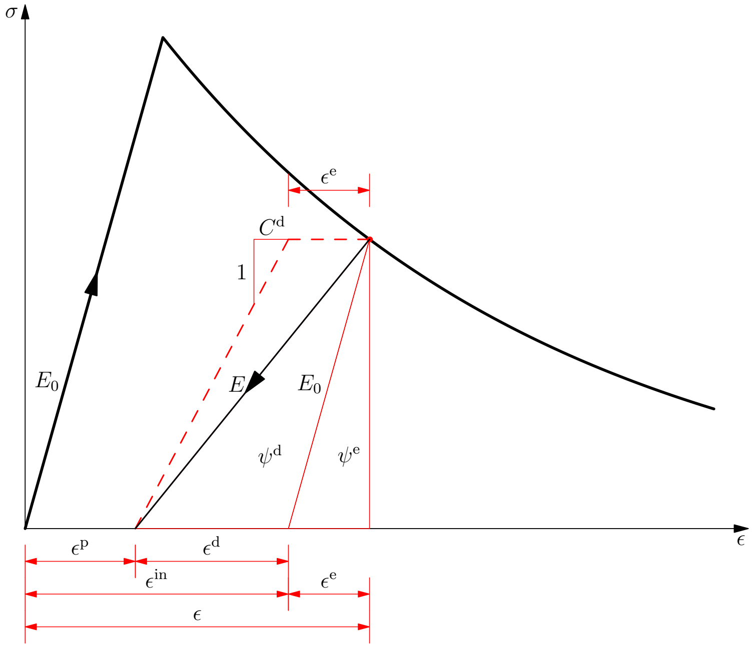

Figure 6: Different kinematic decompositions adopted in the elastoplastic damage/degradation frameworks

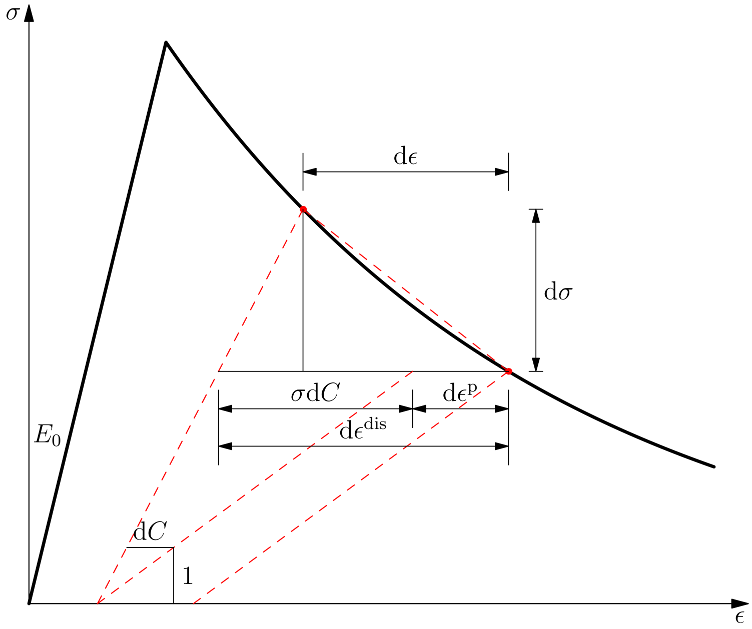

Figure 7: 1D traction-based elastoplatic degradation model

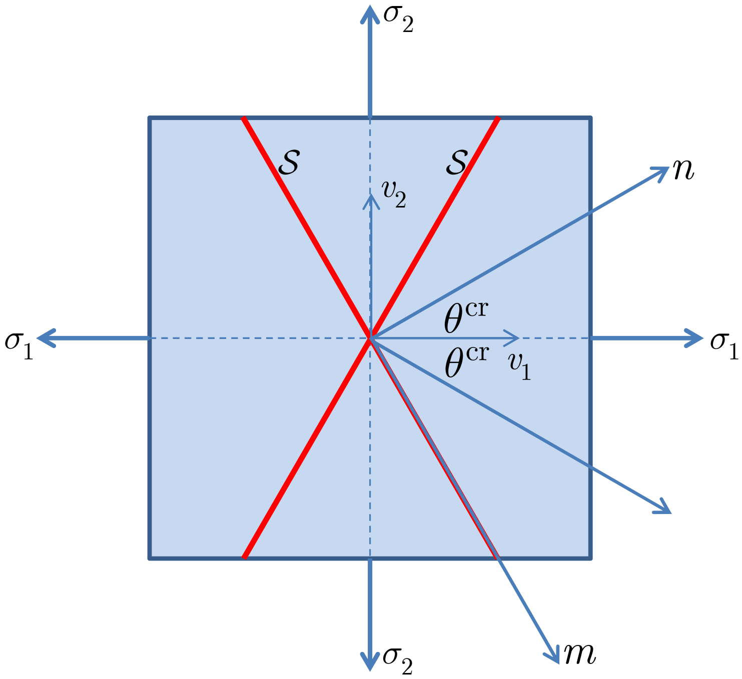

Figure 8: Definition of critical localization angle

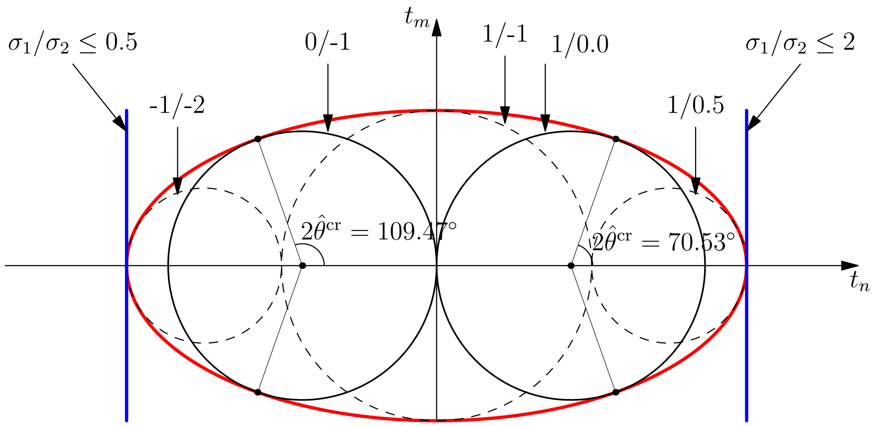

(a) Traction space

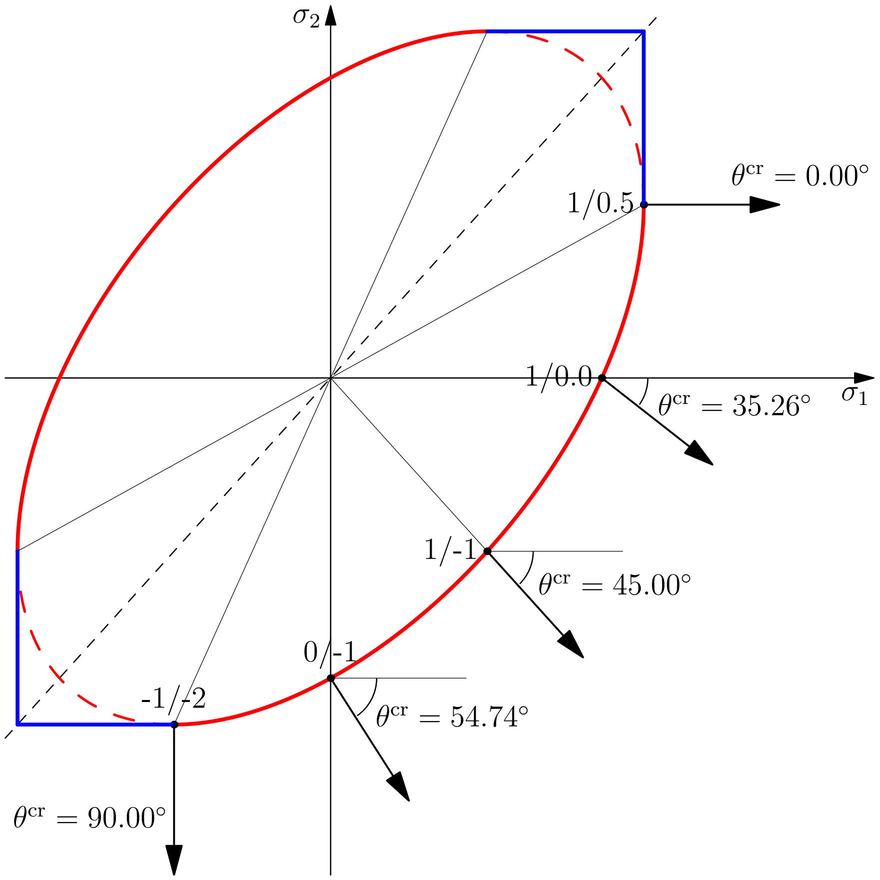

(b) Principal stress space

Figure 9: Discontinuity angles of von Mises criterion in plane stress conditions

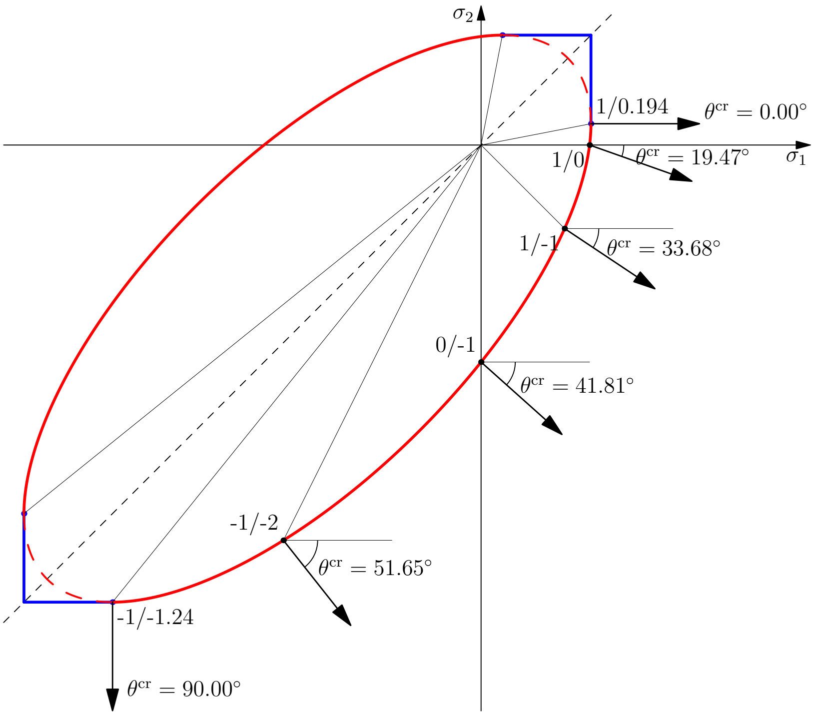

(a) Elliptic type ($\rho = 2.0$)

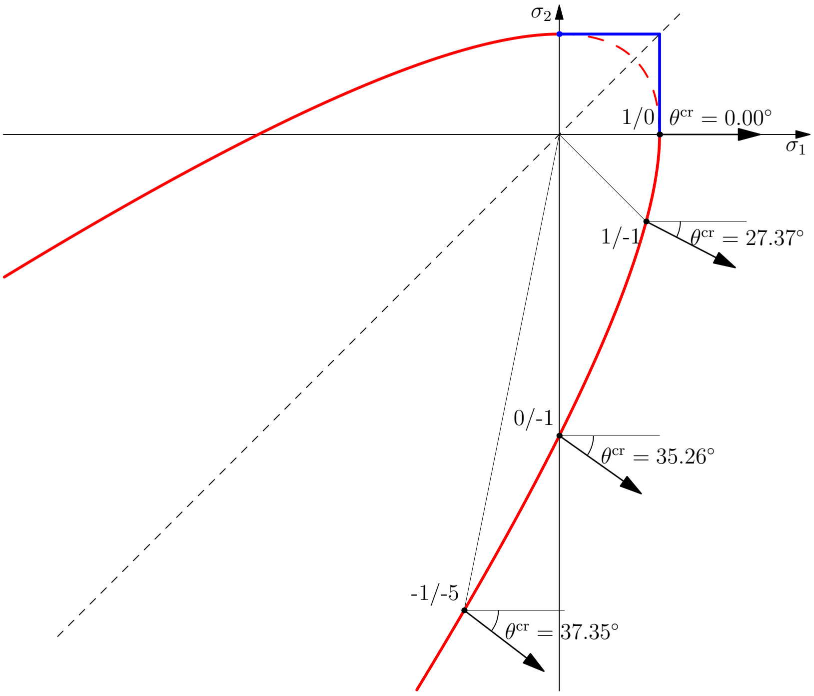

(b) Parabolic type ($\rho = 3.0$)

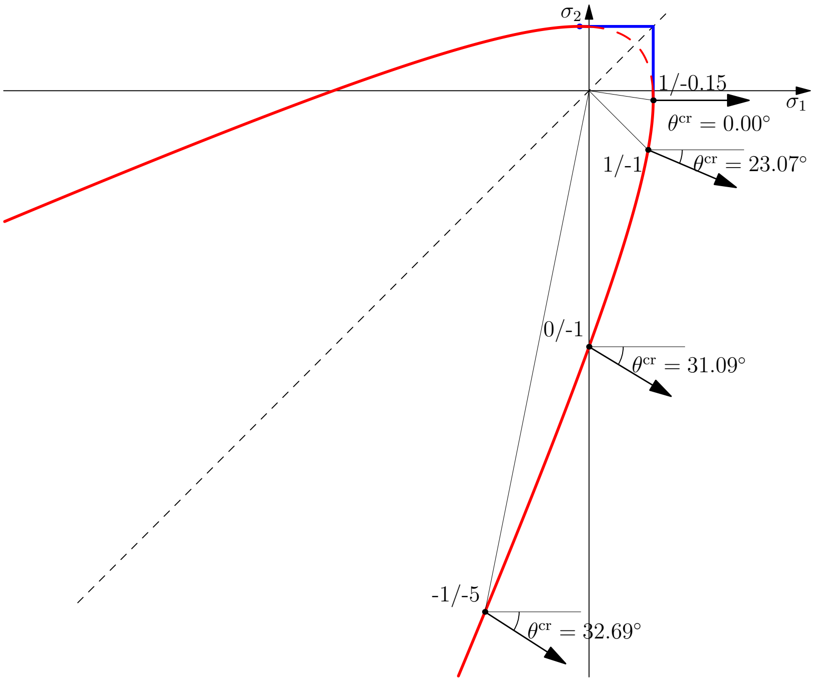

(c) Hyperbolic type ($\rho = 4.0$)

Figure 10: The Drucker-Prager criteria of different types in plane stress conditions

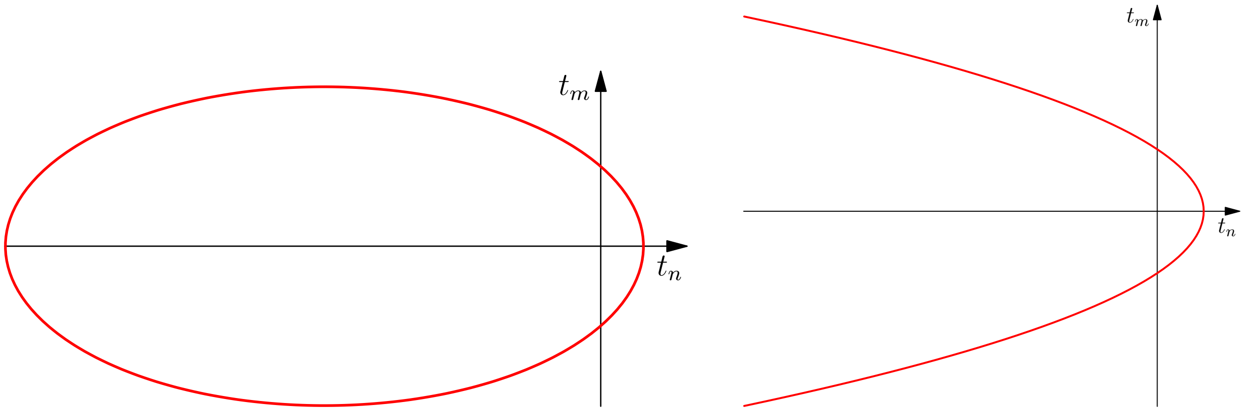

(a) Elliptic failure surface ($\rho = 5.0, A_0 = 0.0$)

(b) Parabolic failure surface ($\rho = 5.0, A_0 = 0.5$)

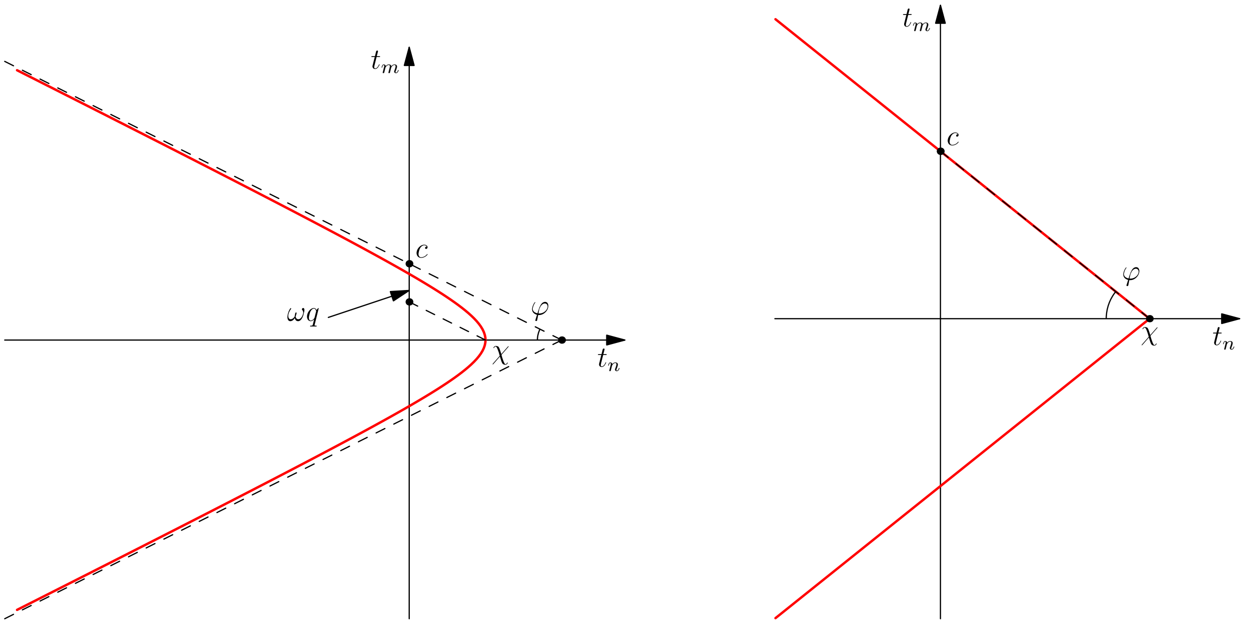

(c) Hyperbolic traction-based failure surface ($\rho = 5.0, A_0 = 1.0$)

(d) Bilinear traction-based failure surface ($\rho = 5.0, A_0 = 7/6$)

Figure 11: Traction-based failure surfaces in plane stress ($\rho = 5.0, A_0 = 1.0$)

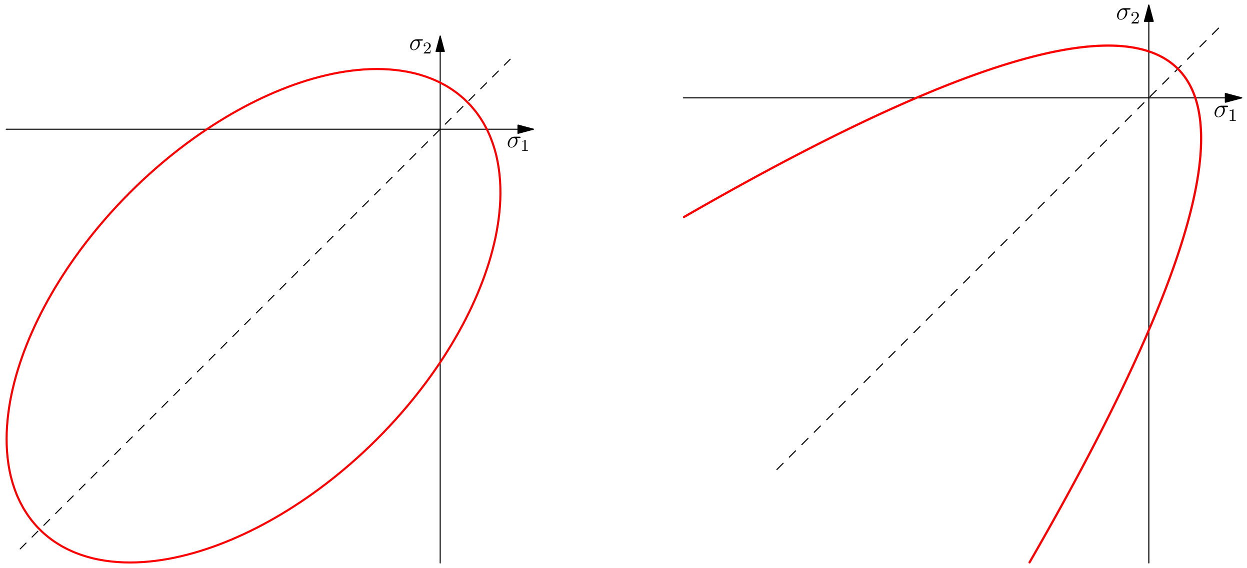

(a) Stress-based failure surface ($\rho = 5.0$, $A_0 = 0.0$) (b) Stress-based failure surface ($\rho = 5.0$, $A_0 = 0.5$)

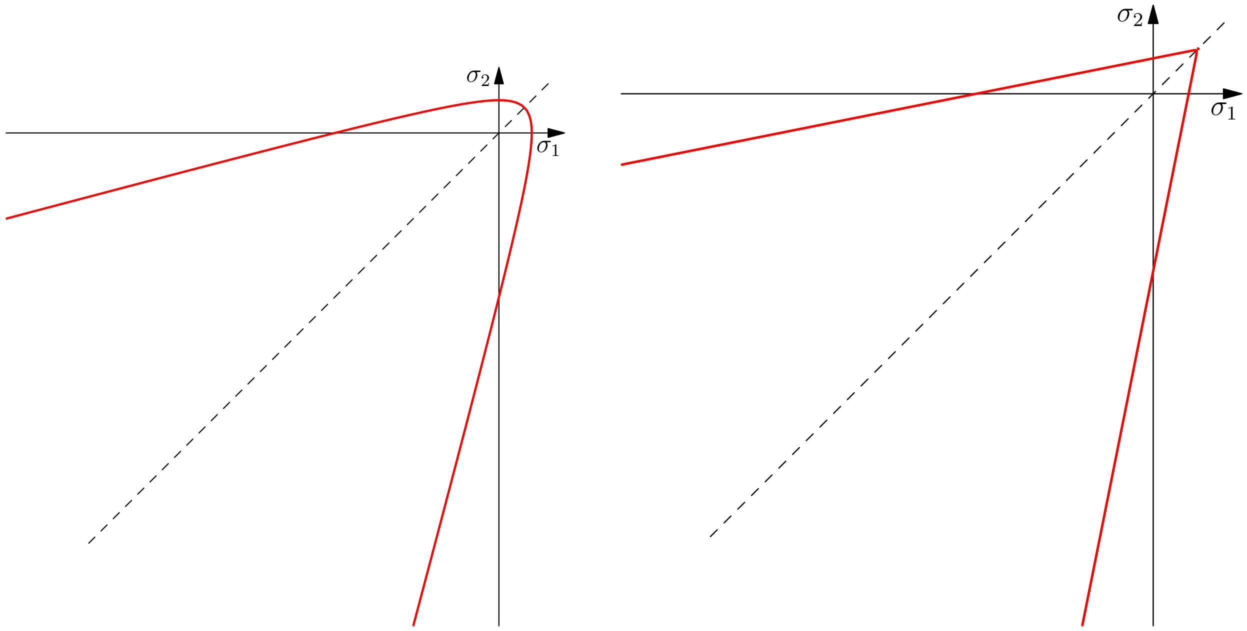

(c) Stress-based failure surface ($\rho = 5.0$, $A_0 = 1.0$) (d) Stress-based failure surface ($\rho = 5.0$, $A_0 = 7/6$)

Figure 12: Stress-based failure surfaces in plane stress

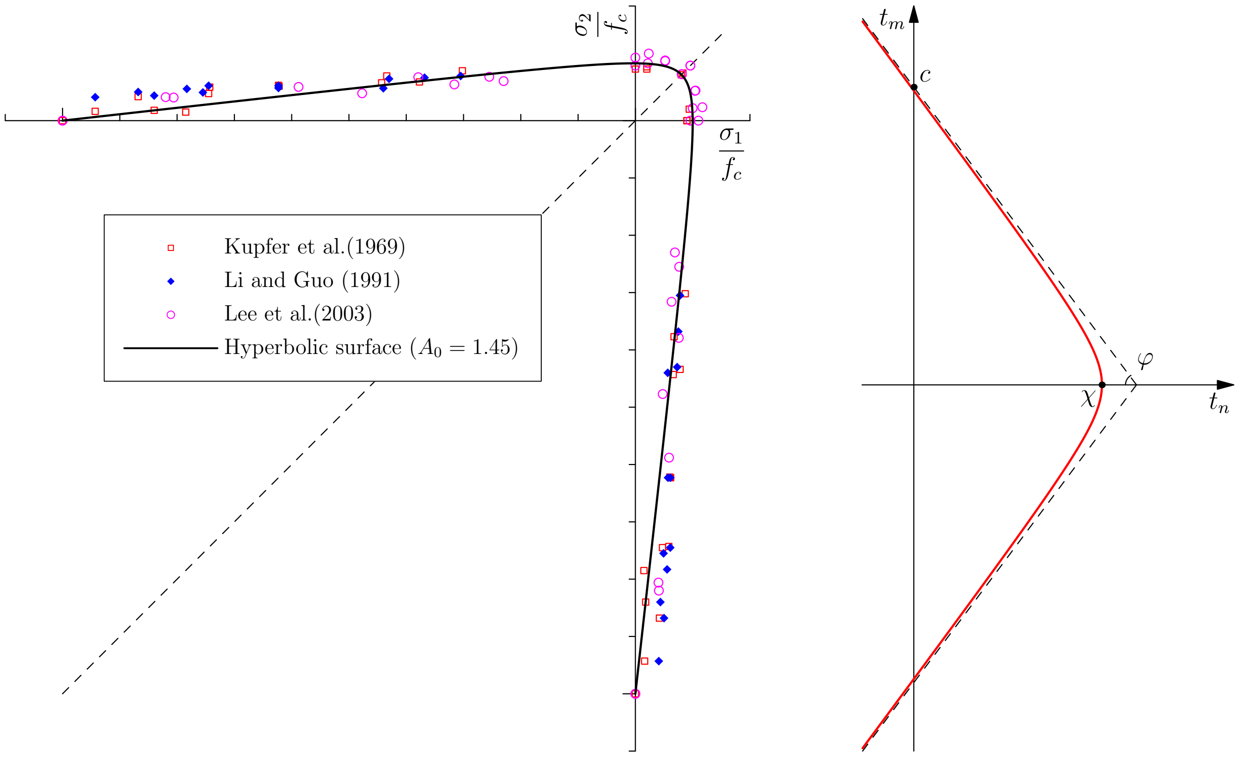

(a) Biaxial strength envelope

(b) Hyperbolic traction-based failure surface

Figure 13: Stress- and traction-based failure surface typical for concrete in plane stress

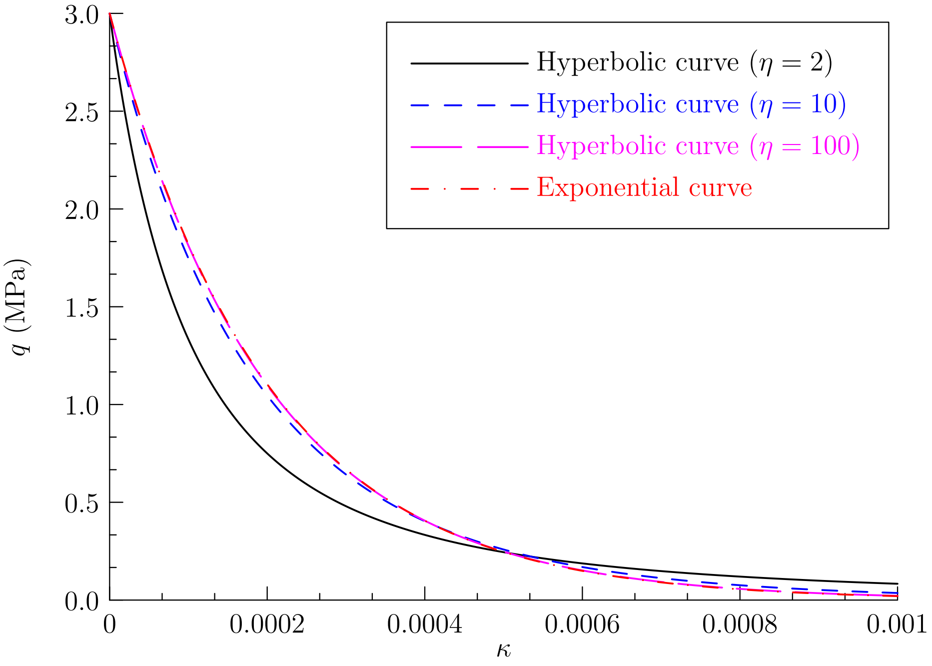

Figure 14: Hyperbolic softening function ($q^0 = 3.0$MPa, $g_f = 600$N/m^2 and $\xi = 0$)

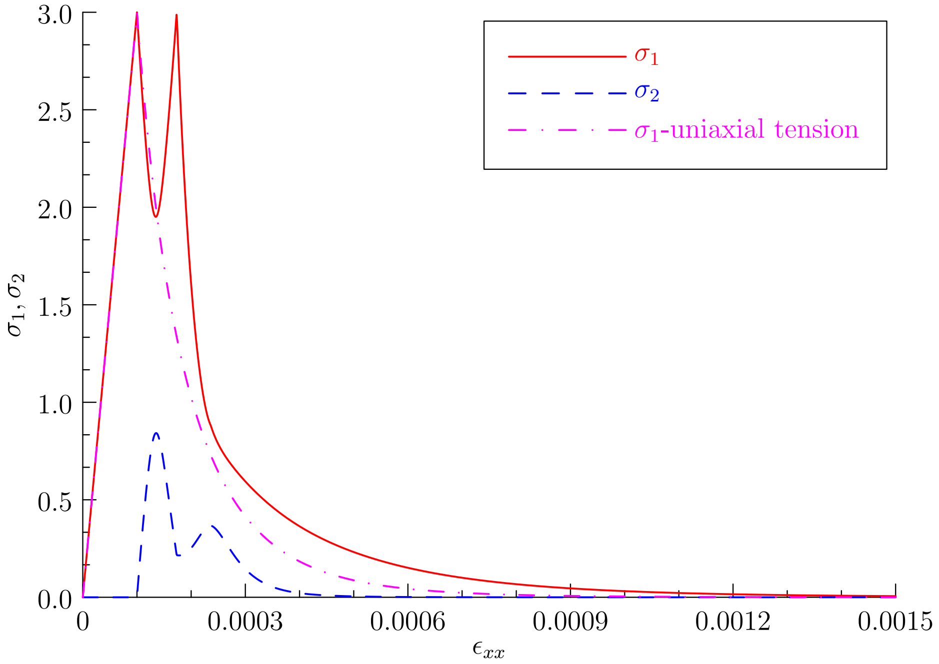

(a) Principal stress components σ_1 and σ_2 versus prescribed normal strain ϵ_{xx}

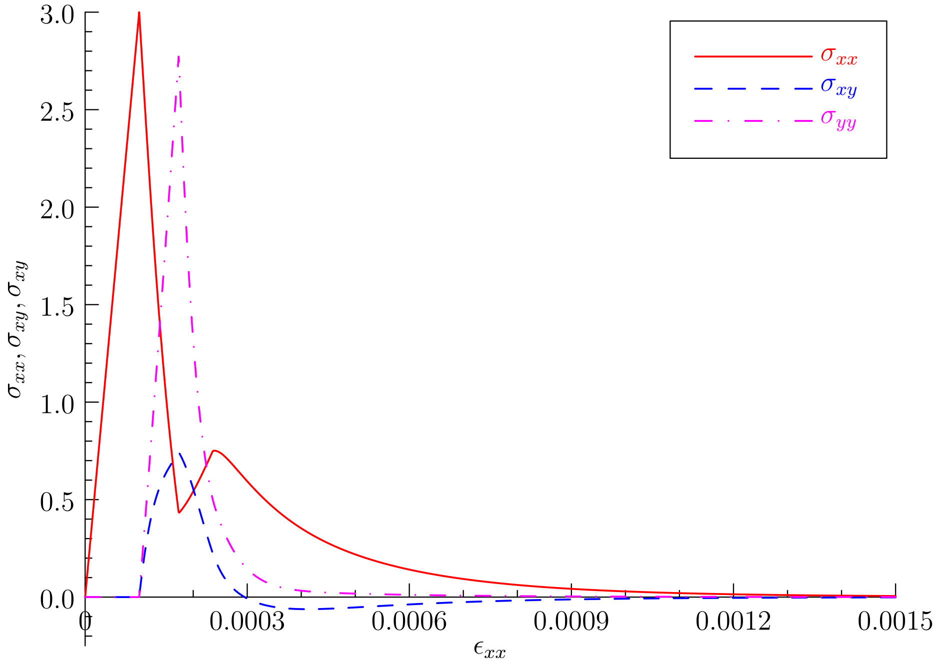

(b) Stress components σ_{xx}, σ_{xy} and σ_{yy} versus prescribed normal strain ϵ_{xx}

Figure 15: Willam's numerical test: evolution of the principal stresses and the stress components.